4-1-2007

Infrared High-Resolution Spectroscopy of Post-AGB Circumstellar Disks. I. HR 4049: The Winnowing Flow Observed?

Kenneth H. Hinkle
National Optical Astronomy Observatory

Sean D. Brittain
Clemson University, sbritt@clemson.edu

David L. Lambert
University of Texas

The Astrophysical Journal, 664:501–517, 2007 July 20

INFRARED HIGH-RESOLUTION SPECTROSCOPY OF POST-AGB CIRCUMSTELLAR DISKS. I. HR 4049: THE WINNOWING FLOW OBSERVED?

Kenneth H. Hinkle
National Optical Astronomy Observatory,[1] P.O. Box 26732, Tucson, AZ 85726-6732; hinkle@noao.edu

Sean D. Brittain[2]
National Optical Astronomy Observatory, P.O. Box 26732, Tucson, AZ 85726-6732; and Department of Physics and Astronomy, Clemson University, Clemson, SC 29634; sbritt@clemson.edu

and

David L. Lambert
W. J. McDonald Observatory, University of Texas, Austin, TX 78712; dll@anchor.as.utexas.edu
Received 2006 April 27; accepted 2007 April 4

ABSTRACT

High-resolution infrared spectroscopy in the 2.3–4.6 μm region is reported for the peculiar A supergiant, single-lined spectroscopic binary HR 4049. Lines from the CO fundamental and first overtone, OH fundamental, and several H_2O vibration-rotation transitions have been observed in the near-infrared spectrum. The spectrum of HR 4049 appears principally in emission through the 3 and 4.6 μm region and in absorption in the 2 μm region. The 4.6 μm spectrum shows a rich "forest" of emission lines. All the spectral lines observed in the 2.3–4.6 μm spectrum are shown to be circumbinary in origin. The presence of OH and H_2O lines confirm the oxygen-rich nature of the circumbinary gas, which is in contrast to the previously detected carbon-rich material. The emission and absorption line profiles show that the circumbinary gas is located in a thin, rotating layer near the dust disk. The properties of the dust and gas circumbinary disk and the spectroscopic orbit yield masses for the individual stars, $M_{\rm A\,I} \sim 0.58\ M_\odot$ and $M_{\rm secondary} \sim 0.34\ M_\odot$. Gas in the disk also has an outward flow with a velocity of $\gtrsim 1$ km s^{-1}. The severe depletion of refractory elements but near-solar abundances of volatile elements observed in HR 4049 results from abundance winnowing. The separation of the volatiles from the grains in the disk and the subsequent accretion by the star are discussed. Contrary to prior reports, the HR 4049 carbon and oxygen isotopic abundances are typical AGB values, $^{12}C/^{13}C = 6^{+9}_{-4}$ and $^{16}O/^{17}O > 200$.

Subject headings: accretion, accretion disks — stars: abundances — stars: AGB and post-AGB — stars: chemically peculiar — stars: evolution — stars: winds, outflows

1. INTRODUCTION

HR 4049 is the prototype for a class of peculiar, post-AGB, single-lined, long-period, spectroscopic binaries (van Winckel et al. 1995). The primary star of these binaries is an early-type supergiant with very peculiar abundances. Most objects in this class exhibit strong infrared excesses of circumstellar origin with carbon-rich circumstellar dust typically present. The combination of carbon-rich material, high luminosity, and location out of the Galactic plane forms the basis for the post-AGB designation. The peculiar designation stems from a photospheric abundance pattern characterized by a severe deficiency of refractory (high dust condensation temperature) elements and a near-solar abundance for volatile (low dust condensation temperature) elements. The abundance anomalies indicate that the present photosphere contains material from which refractory elements have been very largely removed, i.e., a winnowing of dust from gas has occurred.

The basic characteristics of the prototype object HR 4049 are well known. The photosphere has an effective temperature of about 7500 K and shows extreme abundance differences between refractory and volatile elements; for example, HR 4049 has [Fe/H] ~ -4.8 but [S/H] ~ -0.2 (Waelkens et al. 1991b; Takada-Hidai 1990). The orbital period of HR 4049 is 430 days (Waelkens et al. 1991a), leading to a minimum separation between the two stars of 190 $R_\odot$. Bakker et al. (1998) pointed out that the orbit requires a phase of common envelope evolution when the primary was at the tip of the AGB and had a radius of $\sim$250 $R_\odot$. This phase altered the masses and abundances of the components.

The HR 4049 infrared excess is pronounced redward of $\sim$1 μm and is very well fit by a single blackbody at a temperature of about 1150 K and attributed to radiation from the tall inner walls of an optically thick circumbinary disk (Dominik et al. 2003). A circumbinary Keplerian rotating disk appears to be a common feature of the HR 4049 class of post-AGB binaries (De Ruyter et al. 2006). The inner walls of the HR 4049 circumbinary disk are $\sim$10 AU from the binary or 50 times the radius of the supergiant. Our line of sight to the binary nearly grazes the edge of the disk; the angle of inclination of the line of sight to the normal to the disk is about 60°. A cartoon of the system is shown in Figure 1.

Superimposed on the infrared dust continuum are emission features. Waters et al. (1989) detected features due to polycyclic aromatic hydrocarbons (PAHs). This result was confirmed by the *Infrared Space Observatory* (*ISO*) SWS spectrum of Beintema et al. (1996). Geballe et al. (1989) confirmed a C-rich circumstellar environment by detecting 3.43 and 3.53 μm emission features later identified with hydrogen-terminated crystalline facets of diamond (Guillois et al. 1999). Remarkably, Dominik et al.

[1] Operated by Association of Universities for Research in Astronomy, Inc., under cooperative agreement with the National Science Foundation.
[2] Michelson Fellow.

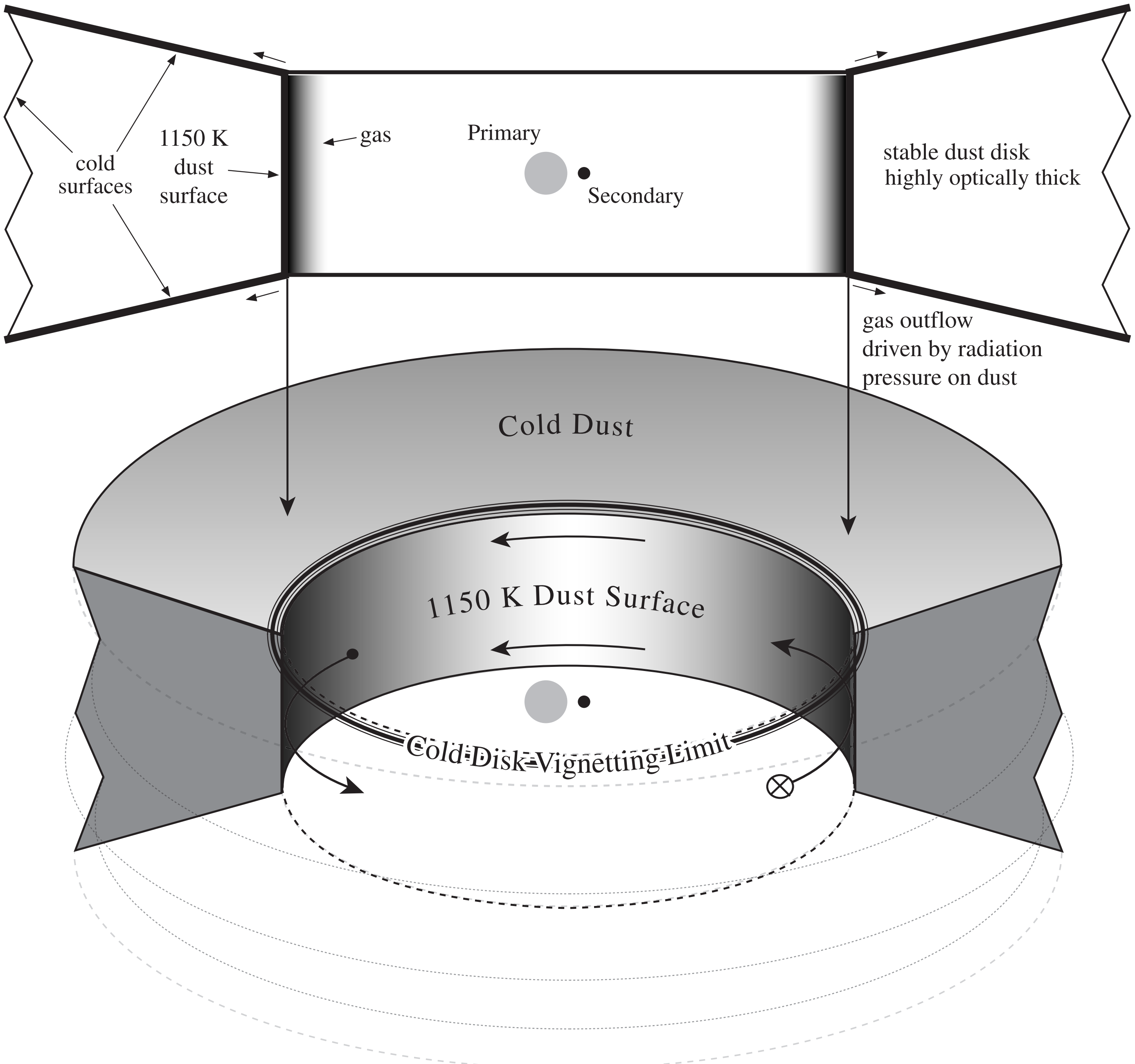

FIG. 1.— Cartoon of the "wall" model for HR 4049 (*top*) taken from Dominik et al. (2003). Below the Dominik model, the spatially resolved observer's view of the system is shown in cross section. The disk is illuminated only from the inside. The cold disk blocks a large section of the inner 1150 K surface from view. The observer sees only that section of the 1150 K disk inside the oval labeled "Cold Disk Vignetting Limit."

(2003) report that the gas molecular species seen in the infrared (*ISO*) spectrum are those expected of an O-rich mixture, suggesting that the HR 4049 circumbinary environment is a blend of C-rich dust and O-rich gas.

Optical spectroscopy offers some information on the disk's gas. Bakker et al. (1998) report changes in the Hα line profile with orbital phase. Bakker et al. (1998, 1996) detected a broad ($\sim$15 km s^{-1}) stationary emission component in the Na I D2 and [O I] 6300 Å lines which they attributed to the circumbinary disk. However, the infrared offers much more readily interpreted signatures of gas in and around the binary. Lambert et al. (1988) detected the $^{12}C^{16}O$ first-overtone spectrum in absorption with an excitation temperature of about 300 K. Cami & Yamamura (2001) on analyzing an *ISO* SWS spectrum of CO_2 emission bands found strong contributions from isotopomers containing ^{17}O and ^{18}O, which they interpreted as $^{16}O/^{17}O = 8.3 \pm 2.3$ and $^{16}O/^{18}O = 6.9 \pm 0.9$.

The origins of the HR 4049 class of chemically peculiar supergiants and the structure of their circumbinary/circumstellar material remain ill understood. New observational attacks appear to be essential. In this paper we report on a detailed look at several regions of the 2–5 μm infrared spectrum of HR 4049.

2. OBSERVATIONS AND DATA REDUCTION

The spectrum HR 4049 was observed at high resolution at a number of near-infrared wavelengths in the 2.3 to 4.6 μm region using the 8 m Gemini South telescope and the NOAO high-resolution near-infrared Phoenix spectrometer (Hinkle et al. 1998,

TABLE 1
Log of Observations

Date	Wavelength (μm)	Frequency (cm^{-1})	S/N
2002 Feb 13..............	2.3120	4324	290
2002 Feb 13..............	2.3233	4303	220
2002 Feb 13..............	2.3309	4289	280
2002 Feb 13..............	2.3421	4268	260
2002 Feb 13..............	2.3617	4233	400
2002 Dec 11..............	2.3405	4272	80
2002 Dec 12	2.3126	4323	90
2002 Dec 12	4.6434	2153	200
2002 Dec 12	4.6629	2144	190
2002 Dec 14	2.2980	4350	350
2002 Dec 14	2.9977	3335	130
2002 Dec 14	4.6219	2163	150
2002 Dec 14	4.6825	2135	170
2003 Feb 16..............	2.3416	4269	210
2004 Apr 3................	4.8874	2045	220
2005 Dec 10	2.3634	4230	300
2005 Dec 10	2.3523	4250	350

2000, 2003). Phoenix is a cryogenically cooled echelle spectrograph that uses order-separating filters to isolate sections of individual echelle orders. The detector is a 1024×1024 InSb Aladdin II array. Phoenix is not cross dispersed, and the size of the detector in the dispersion direction limits the wavelength coverage in a single exposure to about 0.5%, i.e., 1550 km s^{-1}, which is 0.012 μm at 2.3 μm (22 cm^{-1} at 4300 cm^{-1}) and 0.024 μm at 4.6 μm (11 cm^{-1} at 2100 cm^{-1}). One edge of the detector is blemished, so the wavelength coverage is typically trimmed a few percent to avoid this area. Wavelength coverage is limited overall to 0.9–5.5 μm by the InSb detector material. All the spectra discussed here were observed with the widest (0.35″) slit resulting in a spectral resolution of $R = \lambda/\Delta\lambda = 50{,}000$. The central wavelengths of the regions observed are listed in Table 1.

The thermal brilliance of the sky makes observations longward of $\sim$4 μm much more difficult than in the nonthermal 1–2.4 μm region. However, for a bright star like HR 4049, this only slightly increases the already short integration time. Thermal infrared observations were done using standard infrared observing techniques (Joyce 1992). Each observation consists of multiple integrations at several different positions along the slit, typically separated by 4″ on the sky. At thermal infrared wavelengths the telluric lines are in emission. In order not to saturate the telluric emission lines the limiting exposure time is about 30 s at 4.6 μm. For longer integration times, multiple exposures can be co-added in the array controller to make up a single exposure. However, HR 4049 is so bright that total exposure times of only 10–20 s were required. The delivered image FWHM at the spectrograph varied from 0.25″ to 0.80″ during the nights that spectra were taken. With the positions along the slit separated by several arcseconds, the resulting spectral images were well separated on the detector.

An average flat observation minus an average dark observation was divided into each frame observed and frames with the star at different places along the slit were then differenced and the spectrum extracted using standard IRAF[3] routines. A hot star, with no intrinsic spectral lines in the regions observed, was also observed at each wavelength setting. The hot star was observed at air mass near that of HR 4049, and the HR 4049 spectrum was later divided by the hot star spectrum to ratio the telluric spectrum from the HR 4049 star spectrum. Wavelength calibrations were computed by using a set of telluric wavelengths obtained from the hot star spectra. The wavelength calibration yielded residuals of typically 0.25 km s^{-1}.

Observations of HR 4049 were taken in the 2 and 3 μm region as well as the 4.6 μm region. For a bright star the stellar signal is much stronger than background radiation in these spectral regions, and as a result, the observations are much less challenging than 4.6 μm observations. The Phoenix observing technique for this spectral region has previously been described in Smith et al. (2002).

3. ANALYSIS OF THE SPECTRA

Observations of the 2.3, 3.0, and 4.6 μm regions reveal lines from just three molecular species: CO, OH, and H_2O. As discussed in § 1, HR 4049 has a carbon-rich circumstellar envelope, but we did not identify any molecules associated with conditions where C > O. In the 4.6 μm region we searched for C_3 and CN, which should be prominent if C > O. Instead, we report on the new detection of a rich 4.6 μm forest of CO fundamental and H_2O lines. The 4.6 μm region atomic hydrogen lines Pfβ and Huϵ, if present, are blended with H_2O lines. The 4.6 μm HR 4049 emission line spectrum is very rich, making the identification of occasional atomic features problematic. The circumstellar continuum at 4.6 μm is approximately 25 times more intense than the continuum of the supergiant (Dominik et al. 2003), so features of stellar origin will be highly veiled. At 3 μm we make a first detection of the OH fundamental vibration-rotation lines in HR 4049. Before exploring the emission line spectrum, we revisit in § 3.1 the 2.3 μm CO first-overtone spectrum detected previously by Lambert et al. (1988).

All velocities in this paper are heliocentric. In order to compare heliocentric velocities of HR 4049 with microwave observations, add -11.6 km s^{-1} to convert to the local standard of rest.

3.1. CO *First Overtone*

Our observations confirm and extend the discovery of first-overtone ($\Delta v = 2$) vibration-rotation CO lines in absorption (Lambert et al. 1988). At the 2.3 μm wavelength of the CO first overtone, the continuum from the dust is about 4 times that of the supergiant. Thus, the CO absorption lines should be formed along the lines of sight to the circumbinary disk. By inspection (Fig. 2), it is apparent that the rotational and vibrational temperatures are low; high rotational lines of the 2–0 band are absent and the 3–1 (and higher) bands are weak or absent relative to the low rotational lines of the 2–0 band. All of the prominent lines are attributable to the most common isotopic variant, $^{12}C^{16}O$, but weak 2–0 ^{13}CO lines are detectable.[4]

The first set of observations from 2002 February show the CO lines at a radial velocity of -33 ± 0.5 km s^{-1}. The lines reach maximum strength at $J'' \sim 7$, suggesting a rotational excitation temperature of $\sim$300 K. At $J'' = 7$, the *R*-branch lines are about 17% deep and are resolved with a FWHM of 16 km s^{-1} compared to the instrumental resolution of 6 km s^{-1}. Weak ^{13}CO lines are detected with depths for the *R*18–*R*23 lines of about 4%. Comparing lines of similar excitation suggests that $^{12}C/^{13}C \sim 10$. The observed regions cover the strongest predicted $C^{17}O$

[3] The IRAF software is distributed by the National Optical Astronomy Observatories under contract with the National Science Foundation.

[4] We follow the convention of omitting the superscript mass number for the most common isotope. Hence, $^{12}C^{16}O$ appears as CO, etc.

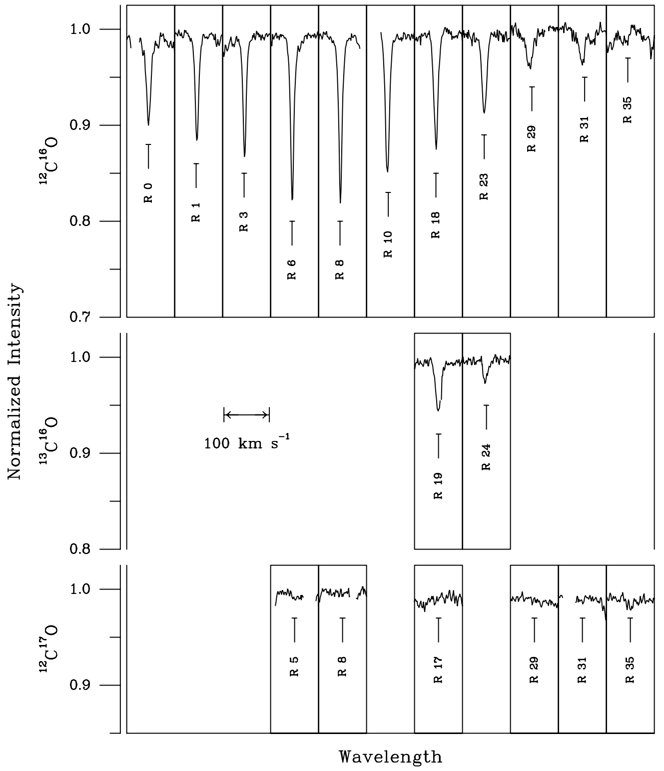

FIG. 2.—Selection of CO 2–0 *R*-branch lines. The abscissa consists of ~8 Å (1.5 cm^{-1} or ~100 km s^{-1}) increments of spectrum centered on each of the labeled lines. *Top*: $^{12}C^{16}O$ lines; *middle*: ^{13}CO lines; *bottom*: $C^{17}O$ lines. The columns align the rotation quantum number *J* for the isotopic lines to approximately equal excitation (within $J'' \pm 1$). The spectral region containing ^{13}CO was not well covered, hence only a few lines are shown; however, ^{13}CO lines are clearly present in the spectrum. Only limits to the $C^{17}O$ lines are detected. All CO first-overtone lines have purely absorption profiles.

lines (2–0 lines near $J'' \sim 7$), but these lines cannot be convincingly identified in the spectra (Fig. 2) demanding $C^{16}O/C^{17}O \gtrsim 100$. A yet more stringent limit can be applied (§ 4) by modeling.

After the original observations, additional data were collected to extend the excitation range of the lines. For instance, observations made in 2002 December included higher *J* lines than observed previously. Observations in 2005 December covered the low-*J P*-branch required for curve-of-growth analysis. Some wavelength intervals were reobserved over the 2002–2005 interval to check for variability. The radial velocity was in all cases unchanged from the −33 km s^{-1} measured in the original data set. This velocity is nearly equal to the -32.09 ± 0.13 km s^{-1} systemic velocity of the spectroscopic binary (Bakker et al. 1998).

The CO first-overtone line profiles are symmetrical with no hint of an emission component. The line strengths showed no temporal variability. In fact, the line intensities are quite similar to those reported by Lambert et al. (1988). Similarly, the velocity is identical to the earlier reported value. The profile of the lowest excitation line, 2–0 *R*0, differs from others in that it possibly has a weak blueshifted component. However, the 2–0 *R*0 line lies in a region with a complex telluric spectrum which is difficult to ratio out of the HR 4049 spectrum. In the 2003 February spectrum, the 2–0 *R*0 line appears to have components at −23.6 and −32.9 km s^{-1}. On other dates, the blueshifted component is less clearly resolved, suggesting that it is either of variable velocity, affected by overlying emission of variable intensity and/or velocity, or a relic of the reduction process. If this blueshifted component exists, it must originate in very cold gas ($T \lesssim 5$ K), because the component is not detectable in the 2–0 *R*1 line.

3.2. CO *Fundamental*

In sharp contrast to the spectrum at 2.3 μm, where a sparse collection of weak absorption lines are found, the spectrum near 4.6 μm is rich in emission lines (Fig. 3). Emission lines were identified from four isotopic variants: CO, ^{13}CO, $C^{17}O$, and $C^{18}O$, with roughly equal intensities for all variants. The rarer isotopic variants $^{13}C^{17}O$, $^{13}C^{18}O$, and ^{14}CO were searched for, but are not present. Absorption below the local continuum is also seen in the profiles of the lowest excitation 1–0 CO lines in this interval. The observed spectral interval provides lines mostly from the 1–0 and 2–1 CO bands, but a few *R*-branch lines of the 3–2 CO band are clearly present. The maximum observable rotational level, $J'' \sim 30$, is similar to that seen in the CO first overtone. Table 2 lists the detected fundamental lines of the four CO isotopic forms.

Blending with other lines of different CO isotopes, vibration-rotation transitions, or H_2O lines is common and results in an apparent variety of profiles. All unblended emission lines are double peaked (see Figs. 4–8). For all but the lowest excitation lines, the blue and red peaks are of similar intensity, but characteristically with the blue peak slightly weaker than the red and occurring at velocities of -38.9 ± 0.4 and -28.4 ± 0.5 km s^{-1}, respectively. The central valley of the emission profile has a velocity of -33.7 ± 0.3 km s^{-1}. Velocities are not dependent on the isotopic species. The observed, i.e., uncorrected for instrumental profile, full-width at zero intensity (FWZI) of the emission profile for the weaker lines is ~27 km s^{-1}, with stronger lines having FWZI up to ~35 km s^{-1}. Because of the high line density, the FWZI is a difficult parameter to measure, and our values carry an uncertainty of several km s^{-1}. The observed full-width at half maximum (FWHM) similarly depends on the line strength, but much less dramatically than the FWZI. Typical FWHM values are ~19 km s^{-1}.

At the observed resolution of $\lambda/\Delta\lambda = 50{,}000$, the instrument profile has a significant impact on the observed line profiles and FWZI. Assuming a Gaussian instrumental profile equal to the 6 km s^{-1} FWHM spectral resolution, deconvolution of this instrumental profile from the observed line profile gives a true FWZI of 18 km s^{-1}. The line profiles are strongly smoothed by the instrumental profile. The observations show blue and red sides of the CO lines rising ~20% above the body of typical CO emission lines with the peak at each edge having a FWHM of ~4 km s^{-1}. For more strongly saturated lines, e.g., low-excitation ^{13}CO lines, the FWHM of the blue and red emission spikes are ~8 km s^{-1}. The intrinsic profile clearly has much stronger emission peaks.

The combined absorption-emission profile for the 1–0 CO lines is shown best by the *R*2 and *R*5 lines (Fig. 9). After allowance for similar blends, the profiles of the CO *R*1, *R*2, *R*3, and *R*4 lines can be judged very similar to that of the *R*5 line. The profile of the *R*0 line is possibly of the same type, but blending is more severe. The *R*5 profile is almost a P Cygni profile, blue absorption accompanied by red emission. However, the absorption component is not strongly blueshifted, but has a velocity very similar to that of the absorption lines in the other fundamental lines and to that of the 2–0 lines.

Absorption below the continuum is seen only in the 1–0 *P*- and *R*-branch CO lines (Figs. 3–8). The observed interval includes the *P*1, *P*2, and *P*3 and *R*0, *R*1, *R*2, *R*3, *R*4, and *R*5 lines with definite absorption below the local continuum seen in all these

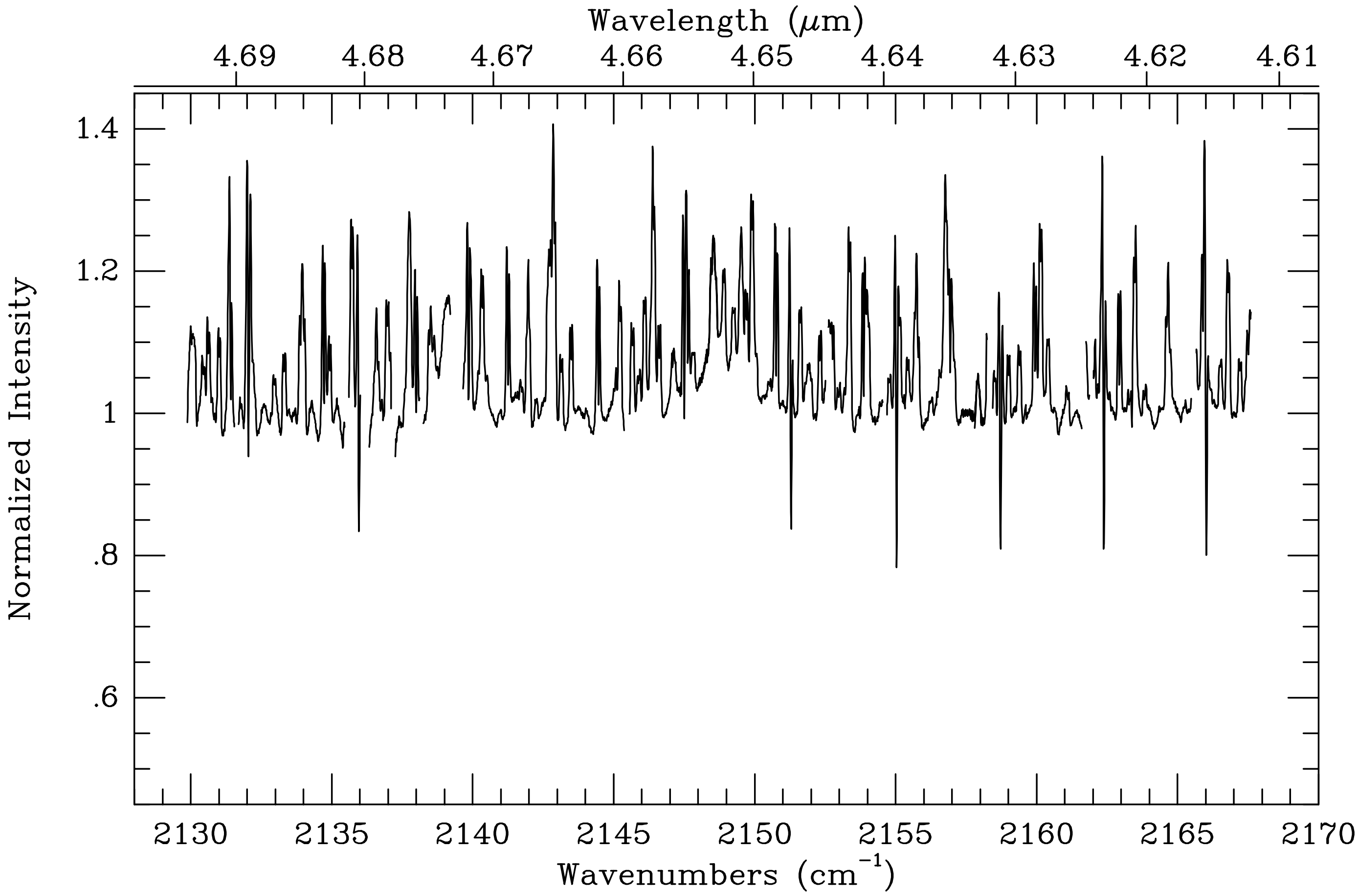

FIG. 3.—Overview of the 4.61–4.69 μm spectrum of HR 4049 showing the forest of CO and H_2O emission lines. Gapped spectral regions indicate failure to restore the spectrum of HR 4049 due to optically thick telluric lines.

TABLE 2
CO $\Delta v = 1$ LINE LIST

Species	Line	i_c[a]	Line	i_c[a]	Line	i_c[a]	Line	i_c[a]
$^{12}C^{16}O$	1–0 *P*3	1.36	1–0 *P*2	1.25	1–0 *P*1	1.27	1–0 *R*0	1.28
	1–0 *R*1	1.26	1–0 *R*2	1.25	1–0 *R*3	1.17	1–0 *R*4	1.36
	1–0 *R*5	1.38						
	2–1 *P*18	1.36	2–1 *R*3	...	2–1 *R*4	1.27	2–1 *R*6	...
	2–1 *R*7	1.37	2–1 *R*8	1.31	2–1 *R*8	1.31	2–1 *R*9	1.26
	2–1 *R*10	...	2–1 *R*11	1.27	2–1 *R*12	1.27	2–1 *R*13	1.22
	3–2 *P*11	1.13	3–2 *R*10	...	3–2 *R*11	1.08	3–2 *R*12	...
	3–2 *R*13	...	3–2 *R*14	1.08	3–2 *R*15	...	3–2 *R*16	...
	3–2 *R*18	...	3–2 *R*21	1.09				
	5–4 *P*5	1.03						
$^{13}C^{16}O$	1–0 *R*9	...	1–0 *R*10	1.23	1–0 *R*11	1.20	1–0 *R*12	1.23
	1–0 *R*13	1.22	1–0 *R*14	...	1–0 *R*15	1.27	1–0 *R*16	1.20
	1–0 *R*17	1.20	1–0 *R*18	1.21	1–0 *R*19	1.17	1–0 *R*20	...
	2–1 *P*7	1.28	2–1 *P*6	1.25	2–1 *R*17	1.12	2–1 *R*18	...
	2–1 *R*19	1.16	2–1 *R*20	...	2–1 *R*21	...	2–1 *R*22	1.13
	2–1 *R*23	...	2–1 *R*24	...	2–1 *R*25	1.13	2–1 *R*26	...
	2–1 *R*27	1.09	2–1 *R*28	...	2–1 *R*29	...	2–1 *R*30	1.08
$^{12}C^{17}O$	1–0 *P*17	1.14	1–0 *R*3	...	1–0 *R*4	1.11	1–0 *R*5	1.15
	1–0 *R*6	...	1–0 *R*8	...	1–0 *R*9	1.12	1–0 *R*10	...
	1–0 *R*11	1.08	1–0 *R*12	...	1–0 *R*13	...		
	2–1 *R*17	...	2–1 *R*19	...				
$^{12}C^{18}O$	1–0 *P*13	1.26	1–0 *P*12	1.24	1–0 *R*10	1.12	1–0 *R*11	1.14
	1–0 *R*12	...	1–0 *R*13	...	1–0 *R*14	1.12	1–0 *R*15	1.12
	1–0 *R*16	1.18	1–0 *R*17	1.13	1–0 *R*18	1.11	1–0 *R*19	...
	1–0 *R*21	1.13	1–0 *R*22	1.12				
	2–1 *R*22	1.03						

NOTE.—Continuum is 1.0.
[a] Intensity of the line measured at the maximum strength of the emission.

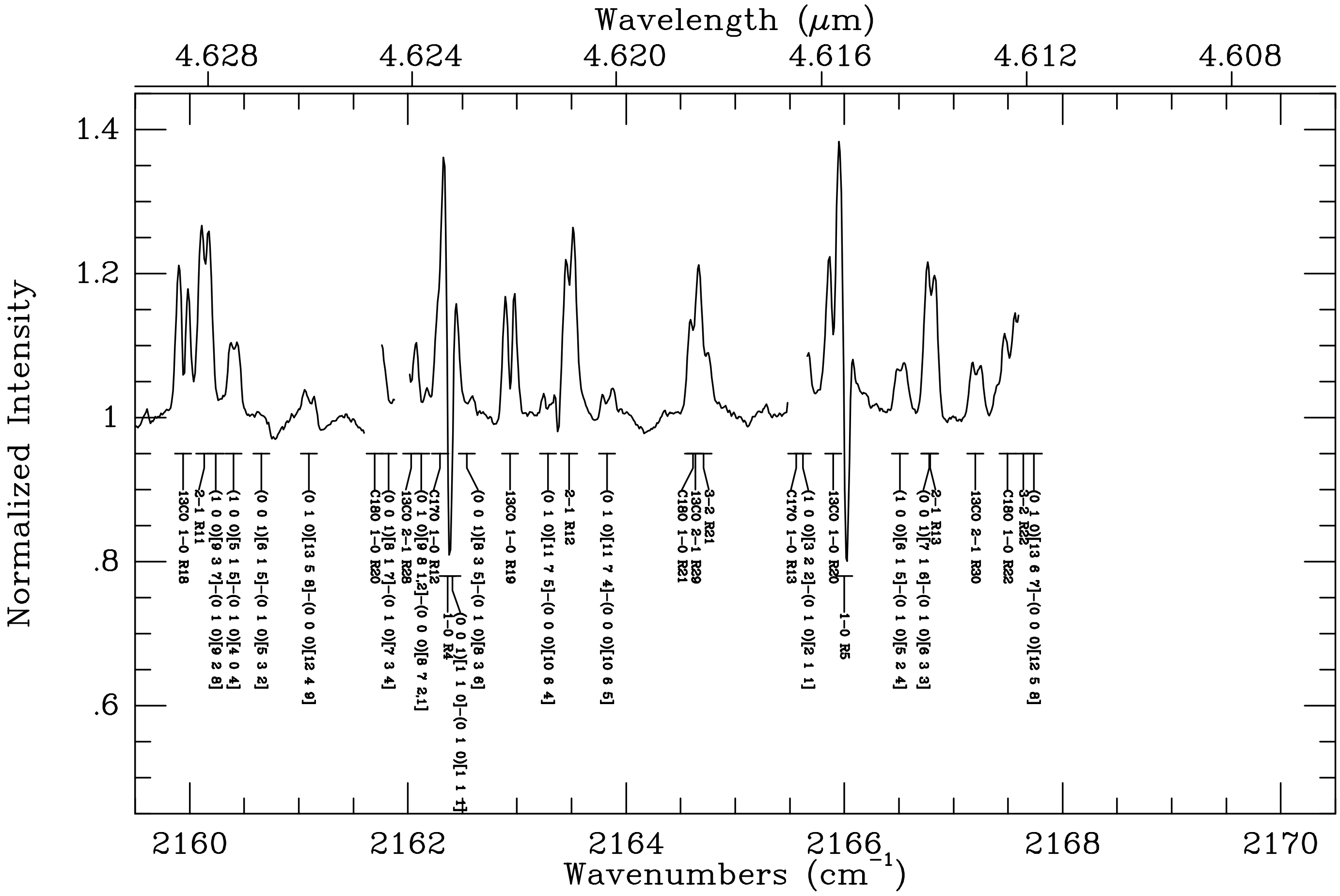

Fig. 4.—The 4.62 μm region spectrum of HR 4049 with line identifications.

lines except $P1$ and $R0$. The strength of the absorption at $R5$ suggests absorption below the local continuum should be detectable to higher J lines of the R-branch. Because of the isotopic shifts, the low-J 1−0 lines of the isotopic variants are not in the observed interval. The lowest member of the R-branch in our spectra is $J'' = 9$ for ^{13}CO, $J'' = 10$ for C^{18}O, and $J'' = 3$ for C^{17}O. All the 1−0 lines regardless of isotopic species have a stronger central valley than the vibrationally excited transitions. The valley almost reaches the local continuum for the 1−0 ^{13}CO lines (note ^{13}CO 1−0 $R10$ and $R11$ in Fig. 7).

The central valley in the line profiles becomes asymmetric for the stronger lines. Self-absorption of the blue emission is obvious when comparing the strength of the blue and red emission in profiles of the 1−0 CO lines (Fig. 9). The 1−0 CO line central absorptions are on average 76% broader on the blue side than the red side. The weaker ^{13}CO 1−0 central absorptions are 20% broader on the blue side. The central absorption is systemically blueshifted relative to the γ-velocity of the binary (Bakker et al. 1998) for the very lowest excitation lines. The shift increases with decreasing J'', with a shift of 1 km s^{-1} for $R5$ and 3.5 km s^{-1} for $R2$ (Fig. 10).

The intensities of the emission lines of CO, ^{13}CO, C^{17}O, and C^{18}O are remarkably similar and quite different from the abundance ratios estimated from the 2−0 lines. Peak intensities of the following representative unblended lines illustrate this point.

CO: 1−0 $R2$ 28%, 2−1 $R11$ 27%, 3−2 $R11$ 11%.
^{13}CO: 1−0 $R12$ 24%, 2−1 $R17$ 14%.
C^{17}O: 1−0 $R11$ 9%, 2−1 $R17$ 14%.
C^{18}O: 1−0 $R14$ 14%.

In contrast to the ratio CO/^{13}CO $\sim$ 10 from the 2−0 lines, the CO/^{13}CO intensity ratio from 1−0 and 2−1 lines of similar J is about 1.5. Even more striking is the appearance of fundamental lines of C^{17}O and C^{18}O with intensities about one-half that of similar lines of CO. Yet, CO/C^{17}O > 100 from the first-overtone lines. The simplest interpretation of these contrasting ratios is that emitting regions are optically thick in all the observed fundamental lines. As is well known, the first-overtone transitions are much weaker than the fundamental lines. Optically thin emission in fundamental and first-overtone lines from a common upper state in the second vibrational level will differ by a factor of about 100 in flux. In the case of absorption from a common state in the ground vibrational level, the absorption coefficient of the 1−0 line is similarly about a factor of 100 stronger than the 2−0 line.

The strengthening of the central absorption for the lowest energy vibrational transition, the asymmetric absorption, and absorption below the continuum require the presence of an absorbing gas cooler than the emitting gas. This absorbing gas has a velocity shifted to the blue of the system barycentric velocity (−32.1 km s^{-1}) by 1−3.5 km s^{-1}. The emitting gas covers a $\sim$18 km s^{-1} range of velocity but is also shifted by $\sim$−1.5 km s^{-1} relative to the barycentric velocity.

3.3. OH *Fundamental*

The lowest excitation OH vibration-rotation 1−0 lines are in a region of considerable telluric obscuration. $J'' = 4.5$ is the

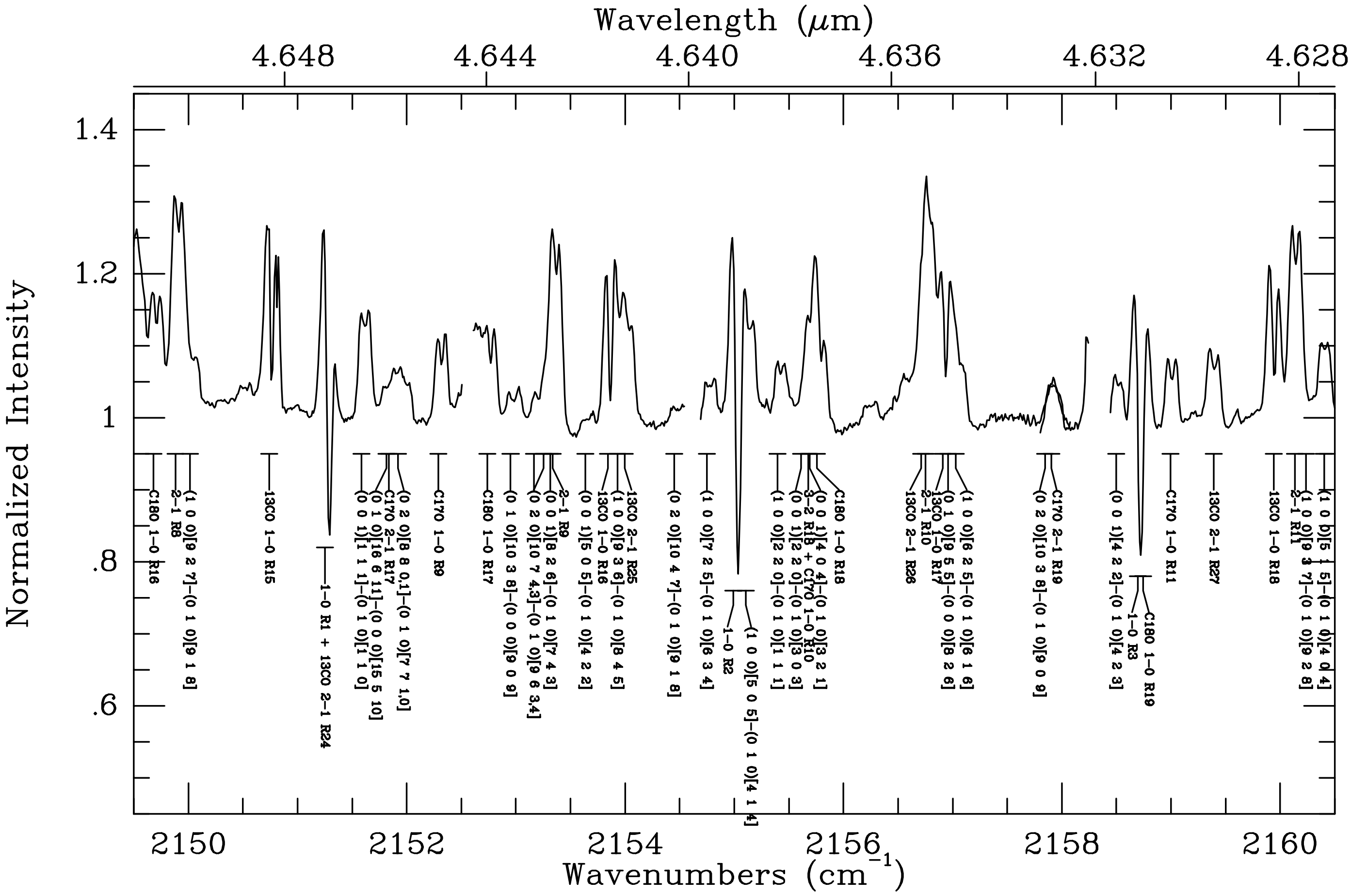

FIG. 5.—Same as Fig. 4, but for the 4.64 μm region.

lowest OH level accessible under typical water vapor conditions (a few mm of precipitable H_2O) at Gemini South. However, a suitable order-sorting filter was not available for the $J'' = 4.5$ wavelength. An observation was made of the *P*-branch line region for $J'' = 5.5$. The $^2\Pi$ OH ground state results in Λ-doubled rotational levels, so each rotational line is divided into four components. As a result, in spite of the large rotational line spacing for OH, several OH lines can appear in a Phoenix spectrum taken with a single grating setting. The 3.0 μm 1–0 $P_{2f}5.5$ and $P_{2e}5.5$ lines were detected in the spectrum of HR 4049 (Fig. 11). This spectral region has considerable telluric absorption. The removal of this absorption results in variable noise in the ratioed spectrum.

The OH lines are, as are the CO lines, seen in emission. The profiles are similar to those of CO with double-peaked profiles of observed FWZI $\sim$ 26 km s^{-1} centered at -35 km s^{-1}. The two OH lines observed are just 5% above the continuum. These were the only lines that were detected in the 3.0 μm spectral region observed.

3.4. H_2O *Vibration-Rotation Lines*

The asymmetric top molecule H_2O is known for the complexity, apparent lack of rotational structure, and richness of its spectrum. As a result, H_2O lines are much more challenging to identify than vibration-rotation lines of simple diatomic molecules (Hinkle & Barnes 1979). Emission lines are clearly present in the 4.6 μm HR 4049 spectrum from three vibration-rotation bands: ν_2, $\nu_1{-}\nu_2$, and $\nu_3{-}\nu_2$. With the above caveats on the H_2O spectrum and based on the tentative identification of four lines, the vibrationally excited band $2\nu_2{-}\nu_2$ might also contribute to the 4.6 μm spectrum. The strongest observed H_2O transitions are from the $\nu_3{-}\nu_2$ band. A number of lines identified with this band have intensities $\sim$20% above continuum. Typical H_2O lines are weaker than typical CO lines, with many of the H_2O lines identified having intensity <10% above continuum.

Table 3 presents a list of the H_2O lines tentatively identified in the HR 4049 spectrum. In Figures 4–9 these lines are labeled on the spectrum of HR 4049. Many lines (e.g., Fig. 9) are unblended and clearly present. However, a fairly large number are blended with CO or other H_2O lines. Because of the overlapping H_2O energy levels, the line strengths of H_2O lines can vary significantly between adjacent vibration-rotational transitions, and hence, the contribution of a H_2O line to a blend is uncertain.

The band strength, S_ν^o, is a factor of 5 lower for the $\nu_1{-}\nu_2$ band than for the $\nu_3{-}\nu_2$ band. However, the band strength for the ν_2 band is more than 10^6 higher than that of either of these bands (McClatchey et al. 1973). The origin of the ν_2 band is $\sim$1.5 μm red of the region observed. While it would be of interest to observe the lowest excitation ν_2 lines, for ground-based observers the telluric ν_2 lines are very strong and prevent observations in the 6 μm region. The $2\nu_2{-}\nu_2$ band has similar band strength to the $\nu_1{-}\nu_2$ and $\nu_3{-}\nu_2$ combination bands, but unlike these bands, which have origins in the regions observed, $2\nu_2{-}\nu_2$ has an origin near that of ν_2. This adds to our suspicion of the $2\nu_2{-}\nu_2$ identifications.

Like CO and OH lines the 4.6 μm H_2O lines have a double-peaked profile with emission peaks at -38.6 and -29.2 km s^{-1} and absorption at -33.6 km s^{-1}. The observed FWZI of the weaker H_2O lines is $\sim$25 km s^{-1}, perhaps slightly narrower than the CO lines.

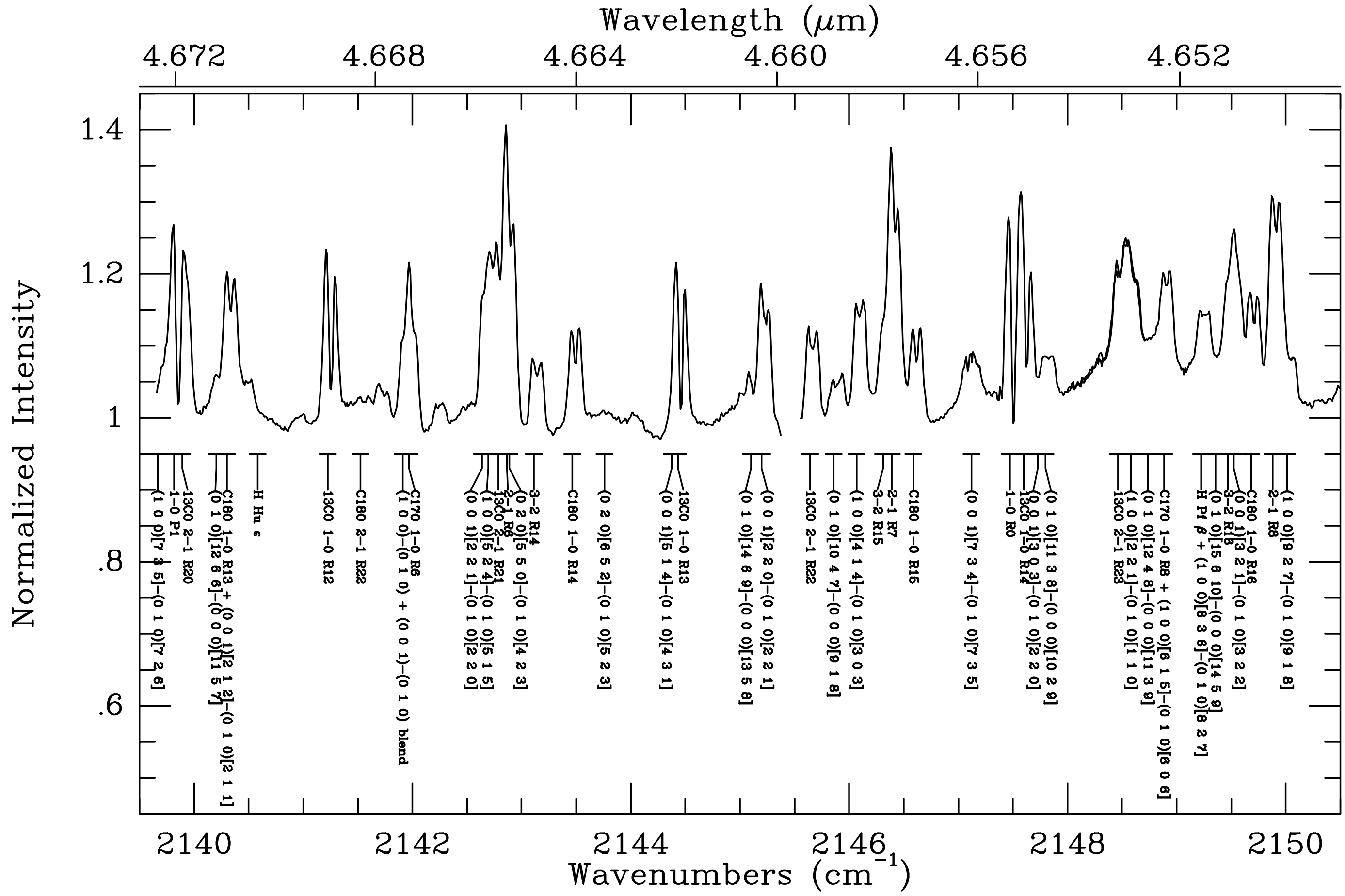

Fig. 6.—Same as Fig. 4, but for the 4.66 μm region.

In addition to the observed 4.6 μm transitions, H_2O also has low-excitation transitions in the 3.0 and 2.3 μm regions. In particular, the ν_3 band crosses the 3 μm region and has a band strength similar to that of the ν_2. The ν_1 band is also present in the 3 μm region and, while weaker than ν_2 or ν_3, is a much stronger transition than the combination bands seen at 4.6 μm. Our 3.0 μm observation has an uneven continuum, perhaps as a result of weak emission features. We undertook a detailed search for H_2O lines but failed to identify any 3.0 μm H_2O lines. Future searches of this region for H_2O lines using higher signal-to-noise ratio data and wider wavelength coverage are justified. On the other hand, our spectra in the 2.3 μm region are of very high quality with broad wavelength coverage, and this region is clearly devoid of any contribution from H_2O.

3.5. *Line Profile Overview*

In summary of the above subsections, CO vibration-rotation fundamental lines of four differently isotopically substituted species and H_2O vibration-rotation lines populate the 4.6 μm region. These lines all have double-peaked emission profiles of total (including both peaks) FWHM ~ 19 km s^{-1}. There is little difference of intensity between lines of different isotopes. The lowest excitation lines, which are only seen in $^{12}C^{16}O$ in the wavelength range observed, have a central absorption as much as 20% below the local continuum. This central absorption overwhelms the bluest of the double peaks in the emission profile, but the extreme bluest edge of the emission remains. Examples of observed CO fundamental and H_2O line profiles are given in Figure 9. OH lines from the fundamental vibration-rotation transition were seen in the 3 μm region. The OH lines are in emission with double-peaked profiles similar to those seen in the CO fundamental and H_2O lines. The CO vibration-rotation first-overtone transition appears in absorption in the 2.3 μm region. The absorption lines are nearly as broad as the CO emission lines, FWHM ~ 16 km s^{-1}, but have simple Gaussian profiles and exhibit a range of line depths suggesting the lines are optically thin. ^{12}CO dominates, but weaker ^{13}CO is detectable. The oxygen isotopes are not present. All spectral lines in the 2–5 μm region have a small ($\gtrsim 1$ km s^{-1}) shift blue of the systemic velocity.

4. MODELING THE MOLECULAR PROBES

The fundamental spectrum presents a difficult analysis task. The CO is seen in both emission and, for the very lowest excitation CO lines, absorption. The small change in intensity for emission lines over the full range of isotopes and over a large range of excitation energy (rotational levels $J'' = 0$ to 30 and vibrational transitions 1–0 to 3–2) clearly indicates that the emission lines are very saturated. A detailed investigation of these strongly saturated lines would require detailed radiative transfer and disk modeling beyond the scope of this paper.

However, analysis of the CO first-overtone lines, which are seen in absorption, is a much more tractable problem. The observations cover nearly all $^{12}C^{16}O$ 2–0 *R*-branch lines from $J'' = 0$ through the highest detectable *R*-branch line at $J'' = 35$. The largest interval of the 2–0 *R*-branch not observed is *R*24–*R*28. The 2–0 *P*-branch was observed from *P*1 through *P*8. The 3–1 *R*-branch from $J'' \geq 4$ also lies in the observed region. Equivalent widths of the first-overtone CO line profiles were

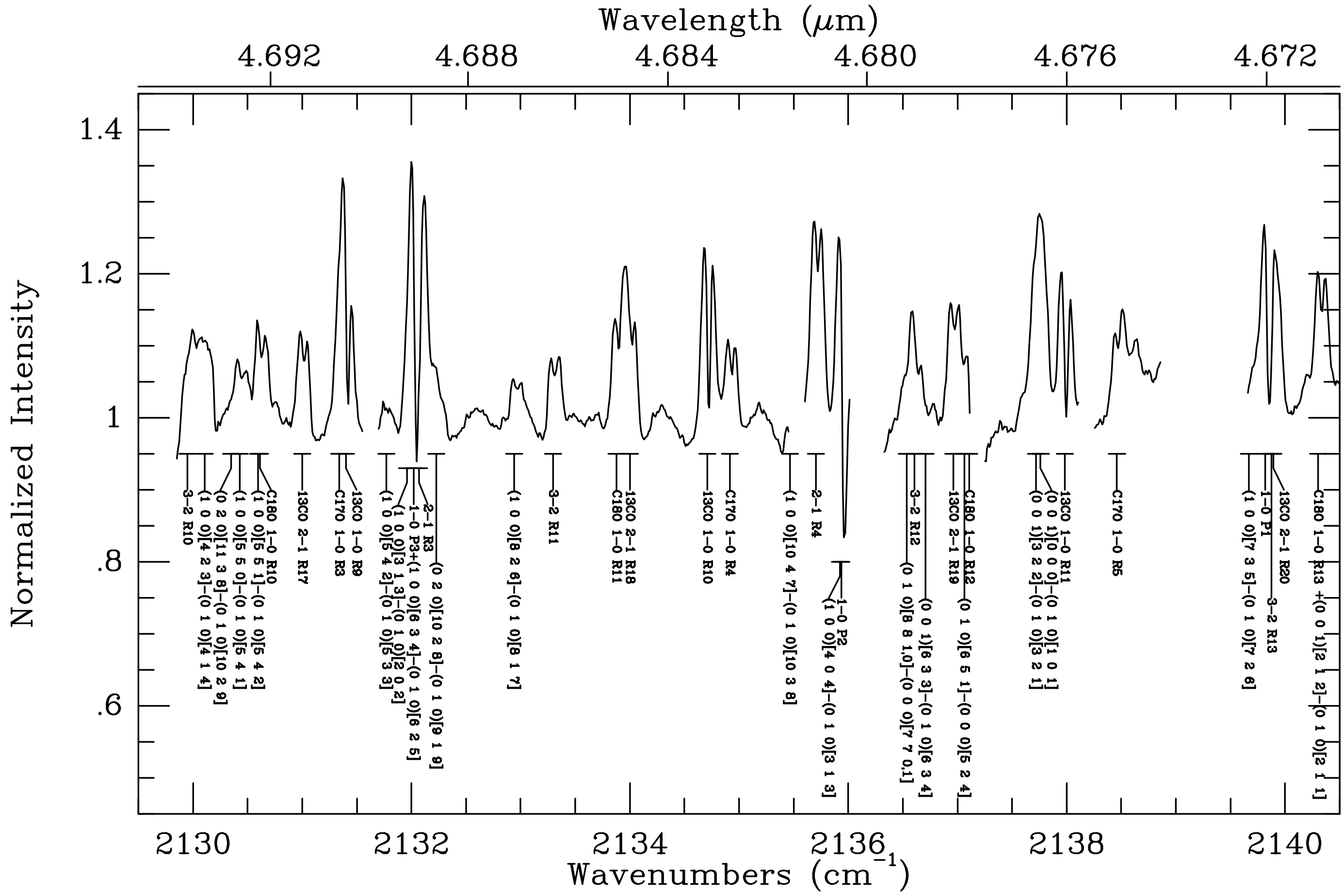

Fig. 7.—Same as Fig. 4, but for the 4.68 μm region.

measured from the fully processed, normalized spectra. The lines were measured both by summing the absorption area and second by Gaussian fits to the line profiles. Uncertainties were estimated from the mean deviations from the Gaussian fits and by the formal uncertainty in the fitted continuum level.

Equivalent-width data were used to produce an excitation plot (Fig. 12). The log-linear increase of line strength with excitation level demonstrates that the high-J $v = 2$–0 lines ($J > 15$) are optically thin (i.e., $\tau < 0.7$). A least-squares fit to the excitation plot of these data requires a temperature of $\sim$550 K. However, the fit to these lines underestimates the column density of the low-J lines. To infer the temperature and optical depth of the low-J lines, we extrapolated the column density of the hot gas (inferred from the high-J lines) and subtracted that from the measured column density.

In order to correct for the effects of saturation, column densities and level populations were determined from a curve-of-growth (COG) analysis (see Spitzer 1978; Brittain et al. 2005), which relates the measured equivalent widths to column densities by taking into account the effects of opacity on a Gaussian line profile. The derived column density for a measured equivalent width only depends on one parameter, the Doppler broadening of the line, $b = \sigma_{\rm rms}/1.665$, where $\sigma_{\rm rms}$ is the rms line width. To find the value of b, we apply two complementary methods: comparison of the P- and R-branch lines and the linearization of the excitation plot. A key assumption is that the small-scale line broadening results entirely from thermal broadening. The resolved line profiles which are seen in the spectra indicate an additional large-scale broadening mechanism which is discussed in § 5.1.

CO exhibits absorption lines in both P ($J'' = J' + 1$) and R ($J'' = J' - 1$) branches, which have different oscillator strengths yet probe the same energy levels, e.g., the $P1$ absorption line originates from the same $J = 1$ level as the $R1$ absorption line. Any differences in the column density derived from lines that share a common level must be due to optical depth, which is related to b. The line width, b, can be used to determine the optical depth and adjusted so that the derived level populations from the two branches agree as closely as possible.

The ($v = 0$, low-J) transitions are thermalized at densities as low as $n_{\rm H} \sim 10^3$–10^4 cm^{-3} and at even lower densities due to radiative trapping in the rotational lines with high opacity. Therefore, the low-J lines are the ones most likely to exhibit a thermal population distribution. The line width that best linearizes a plot of the level populations to a common temperature in an excitation diagram is used.

Subject to the above constraints, the best-fitting b-value in the COG analysis for HR 4049 is 0.5 ± 0.1 km s^{-1}. The consistency of all data to this common velocity dispersion is depicted in the excitation plot of Figure 12. With a measurement of b, equivalent widths can be directly related to column density. The column density from fitting the 2–0 "high-J" lines is $(4.6 \pm 0.3) \times 10^{17}$ cm^{-2} at a temperature of 530 ± 20 K. The column density of the "low-J" lines is $(1.6 \pm 0.2) \times 10^{18}$ cm^{-2} at a temperature of 40 ± 10 K. Uncertainty in the hot $N(^{12}CO)$ from the overtone lines, estimated from the measurement of unsaturated lines, is small and dominated by measurement errors in the equivalent widths of the lines. The uncertainty in the cold gas is dominated by the uncertainty in b. Assuming that the 0.5 km s^{-1} b-value for

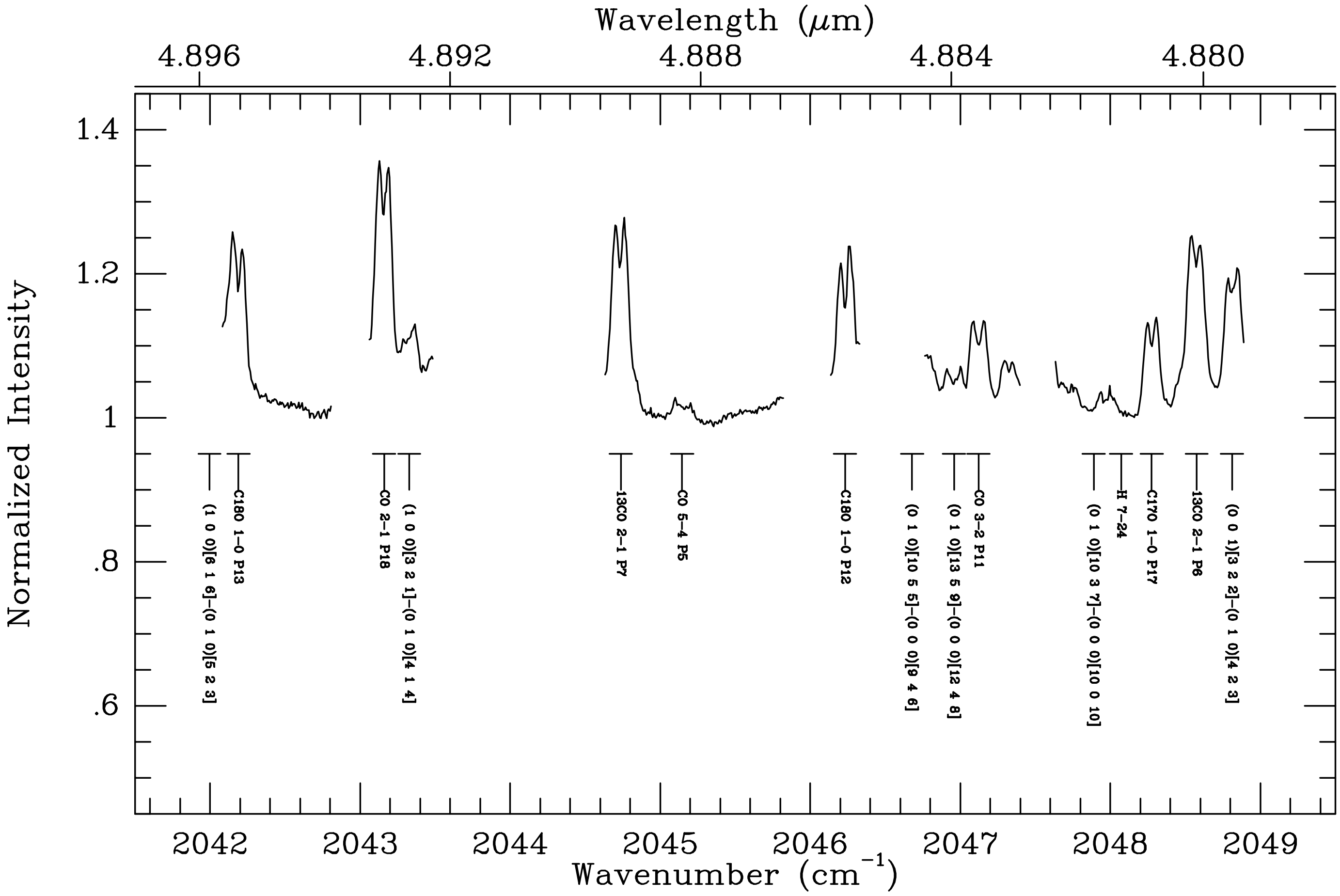

FIG. 8.—Same as Fig. 4, but for the 4.89 μm region.

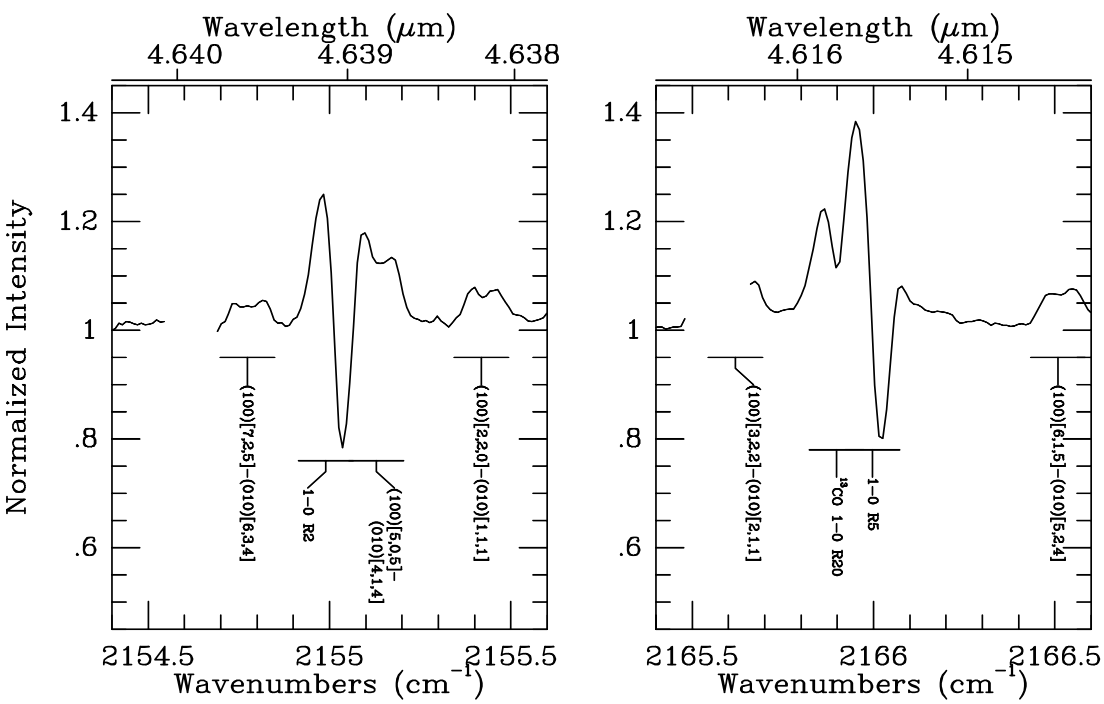

FIG. 9.—Enlarged view of the spectrum shown in Figs. 4 and 5 showing the regions surrounding (*left*) the $^{12}C^{16}O$ *R*2 line and (*right*) the *R*5 line. The *R*2 line is unblended on the red wing while the *R*5 line is unblended on the blue wing. Both lines have P Cygni type profiles. Higher excitation CO lines as well as H_2O lines shown in this figure exhibit typical double-peaked emission profiles.

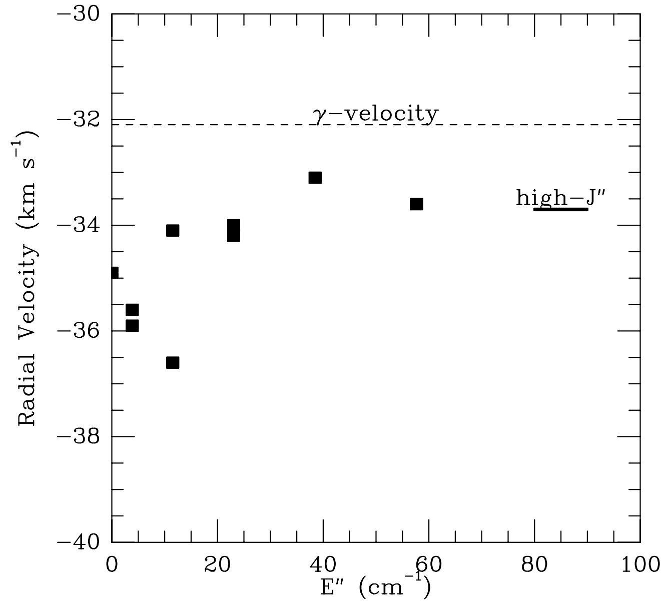

FIG. 10.—Radial velocities of the absorption component of the CO 1−0 low-excitation lines ($J'' = 0$–5) as a function of excitation energy of the lower level. A number of these lines are blended with other circumstellar lines. The bar to the right labeled "high-J''" is at the value of the mid-emission absorption for higher excitation lines. There is a clear trend for the lowest excitation lines to have a larger outflow. The dashed line is the binary system γ-velocity (Bakker et al. 1998).

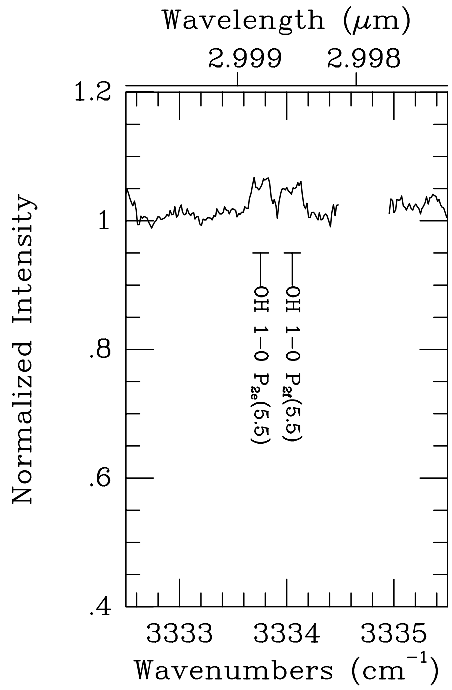

FIG. 11.—The 3 μm region spectrum of HR 4049 showing the OH 1−0 P_{2f}5.5 and 1−0 P_{2e}5.5 lines.

the cold gas applies to all the spectral lines, the opacity of the most optically thick line is ~1.5. Increasing the b-value for the hot gas lowers the optical thickness of the higher excitation lines.

The detection of weak 3−1 lines allows a check on vibrational local thermodynamic equilibrium (LTE) in the gas. The column of CO in the $v = 1$ state (from the $v = 3$−1 lines) is $(5.7 \pm 1.3) \times 10^{15}$, and the temperature is 540 ± 80 K. This is consistent with the temperature for the hot component of the $v = 0$ ^{12}CO and ^{13}CO branches (530 ± 20 and 570 ± 40, respectively). The combined 2−0 and 3−1 data give a rotational temperature of 620 ± 20 K. The vibrational temperature is 700 ± 50 K. This is consistent with a slight overpopulation of the $v = 1$ state, although the relative rotational populations are consistent. The vibrational temperature is more uncertain than the other temperatures and evidence for non-LTE populations is weak.

Using the best-fitting b-value, the column density can be determined for other isotopic lines in the spectrum. The corresponding column density of ^{13}CO is $(2.3 \pm 0.3) \times 10^{17}$ cm^{-2} at a temperature of 570 ± 40 K. Comparing lines of similar excitation, ^{12}C/^{13}C ratio is 6^{+9}_{-4}. First-overtone C^{17}O lines could not be detected. The strongest lines, assuming a 550 K excitation temperature, that are clear of both major telluric features and blending CO lines are R5 and R8 (Fig. 2). A firm upper limit on the equivalent width of these lines is 1.7 mÅ, which translates to a column density of 6×10^{14} cm^{-2}. At a temperature of 550 K, this corresponds to a total column density of C^{17}O of less than 1×10^{16} cm^{-2}. Allowing for the temperature uncertainty, a 3 σ limit for ^{16}O/^{17}O is >200.

5. DISCUSSION

The basic characteristics of the HR 4049 system are well understood. At the heart of HR 4049 is a single-lined spectroscopic binary (Bakker et al. 1998). The visible early-A/late-B supergiant is a low-mass, perhaps white dwarf–mass, post-AGB star. The unseen companion is an M dwarf or white dwarf of lower mass than the supergiant. The infrared prominent feature of the HR 4049 system is the circumbinary shell. Antoniucci et al. (2005) review the various geometries proposed for the circumbinary material. Considerable evidence now points to a thick disk geometry. Detailed arguments are presented by Dominik et al. (2003).

In the following discussion we adopt the Dominik et al. (2003) disk model (Fig. 1) with the following key points. The disk is optically thick with a height-to-radius ratio $\sim\frac{1}{3}$. The dust on the interior disk surface facing the star is approximately isothermal at 1150 K. The temperature of the dust wall implies a distance between the star and dust of ~10 AU. The variability of HR 4049 and the hydrostatic scale height suggest that the inclination of the disk is ~60° (i.e., the plane of the disk is tipped 30° from the line of sight). The optical depth of the dust, the height of the disk, and the inclination result in only the far side of the disk being observable (Fig. 1).

5.1. *Circumbinary Flow*

Previous observations of the CO first overtone are reported by Lambert et al. (1988). Based on an excitation temperature of 300 ± 100 K and a nonstellar velocity Lambert et al. (1988) conclude the CO is circumstellar. The much higher resolution and S/N data analyzed above refine the excitation temperature to 520 ± 20 K for the higher excitation lines and 40 ± 10 K for the low-excitation lines. The velocities reported here and those reported by Lambert et al. (1988) show no change over nearly 20 years, as expected for lines of circumbinary origin. Although the current data are of higher precision, both data sets are consistent with an outflow velocity of ~1 km s^{-1}. The column densities reveal that about 4 times more cool gas, $\sim 2 \times 10^{18}$ cm^{-2}, is present than hot gas, $\sim 5 \times 10^{17}$ cm^{-2}.

The observations demonstrate that the gas is in rotational LTE and near or in vibrational LTE. For vibrational equilibrium the critical density is $n_{\rm H} \sim 10^{10}$ cm^{-3} (Najita et al. 1996). Taking this density and a CO column density of 2×10^{18} cm^{-2}, the

TABLE 3
H_2O Line List

Vibrational Transition	Rotational Transition	i_c[a]	Rotational Transition	i_c[a]	Rotational Transition	i_c[a]
(100)–(010)................	[2,2,0]–[1,1,1]	1.07	[2,2,1]–[1,1,0]	1.19	[3,1,3]–[2,0,2]	. . .
	[3,2,1]–[4,1,4]	1.13	[3,2,2]–[2,1,1]	. . .	[4,0,4]–[3,1,3]	. . .
	[4,1,4]–[3,0,3]	1.16	[4,2,3]–[4,1,4]	1.11	[5,0,5]–[4,1,4]	1.13
	[5,1,5]–[4,0,4]	1.10	[5,2,4]–[5,1,5]	. . .	[5,4,2]–[5,3,3]	1.03
	[5,5,0]–[5,4,1]	1.06	[5,5,1]–[5,4,2]	. . .	[6,1,5]–[5,2,4]	1.08
	[6,1,5]–[6,0,6]	. . .	[6,2,5]–[6,1,6]	1.07	[6,3,4]–[6,2,5]	. . .
	[7,2,5]–[6,3,4]	1.05	[7,3,5]–[7,2,6]	1.07	[8,2,6]–[8,1,7]	1.05
	[8,3,6]–[8,2,7]	. . .	[9,2,7]–[9,1,8]	1.08	[9,3,6]–[8,4,5]	. . .
	[9,3,7]–[9,2,8]	. . .	[10,4,7]–[10,3,8]	1.03		
(010)–(000)................	[6,5,1]–[5,2,4]	. . .	[8,8,1&0]–[7,7,0&1]	. . .	[9,5,5]–[8,2,6]	. . .
	[9,8,1&2]–[8,7,2&1]	1.04	[10,3,7]–[10,0,10]	1.02	[10,3,8]–[9,0,9]	1.04
	[10,4,7]–[9,1,8]	1.06	[11,3,8]–[10,2,9]	1.08	[11,7,4]–[10,6,5]	1.04
	[11,7,5]–[10,6,4]	1.03	[12,4,8]–[11,3,9]	. . .	[12,6,6]–[11,5,7]	1.06
	[13,5,8]–[12,4,9]	1.05	[13,5,9]–[12,4,8]	1.07	[13,6,7]–[12,5,8]	. . .
	[14,6,9]–[13,5,8]	1.06	[15,6,10]–[14,5,9]	. . .	[16,6,11]–[15,5,10]	. . .
(001)–(010)................	[0,0,0]–[1,0,1]	. . .	[1,1,0]–[1,1,1]	. . .	[1,1,1]–[1,1,0]	1.15
	[2,1,2]–[2,1,1]	. . .	[2,2,0]–[2,2,1]	1.18	[2,2,0]–[3,0,3]	. . .
	[2,2,1]–[2,2,0]	. . .	[3,0,3]–[2,2,0]	1.20	[3,2,1]–[3,2,2]	. . .
	[3,2,2]–[3,2,1]	1.23:	[3,2,2]–[4,2,3]	1.21	[4,0,4]–[3,2,1]	. . .
	[4,2,2]–[4,2,3]	1.06	[5,0,5]–[4,2,2]	1.02	[5,1,4]–[4,3,1]	. . .
	[6,1,5]–[5,3,2]	1.01	[6,3,3]–[6,3,4]	1.02	[7,1,6]–[6,3,3]	. . .
	[7,3,4]–[7,3,5]	1.09	[8,1,7]–[7,3,4]	. . .	[8,2,6]–[7,4,3]	. . .
	[8,3,5]–[8,3,6]	1.03				
(020)–(010)................	[5,5,0]–[4,2,3]	. . .	[6,5,2]–[5,2,3]	1.01	[8,8,0&1]–[7,7,1&0]	1.05
	[10,2,8]–[9,1,9]	. . .	[10,3,8]–[9,0,9]	. . .	[10,4,7]–[9,1,8]	1.02
	[10,7,4]–[9,6,3]	1.03	[10,7,3]–[9,6,4]	. . .	[11,3,8]–[10,2,9]	. . .

[a] Intensity of the line measured at the maximum strength of the emission.

thickness of the CO absorption line–forming region is $\sim 4 \times 10^{11}$ cm. So the gas is restricted to a zone radially $\sim 6\ R_\odot$ from the disk inner dust wall. The CO appears to depart slightly from vibrational LTE, so the density is likely slightly lower than the critical density. In any case, the thickness of the gas layer is certainly thin compared to the $\sim 2150\ R_\odot$ spacing between the binary and dust wall.

If the gas layer is located radially just on the star side of the dust wall, adopting the Dominik et al. (2003) geometry permits the total gas mass to be calculated. Taking the radius to be 10 AU and the height of the disk to be one-third of the radius, the surface area of the cylindrical wall follows. The column density then gives the total number of CO molecules. Since the gas is oxygen-rich, the number of CO molecules is limited by the carbon abundance. Taking [C/H] for HR 4049 from Waelkens et al. (1996) and the solar carbon abundance of Grevesse et al. (1991), the mass of the gas disk is 6×10^{26} g, i.e., $\sim 0.1\ M_\oplus$. A total disk mass of a $\gtrsim 33\ M_\oplus$ was suggested by Dominik et al. (2003) so the mass estimates are in accord with a thin gas zone at the edge of a more massive dust disk.

The CO first-overtone lines are symmetric and ~ 16 km s^{-1} across. In contrast, a line width 20 times smaller, ~ 0.5 km s^{-1}, is required to model the curve of growth. A 0.5 km s^{-1} width is consistent with thermal broadening. We suggest that the broadening to 16 km s^{-1} is due to a systemic flow of gas in the circumstellar shell. As noted above, our view of the dust disk continuum is limited to the side opposite from the star (Fig. 1), so many kinds of axisymmetric flows could result in the observed line broadening. We consider the line shapes to constrain further our understanding of the flow.

All the unblended 4.6 μm emission line profiles, including those for weaker lines, are double peaked. Since *all* the lines are double peaked, we discount self-absorption as the principal cause for this line shape. Double-peaked lines suggest an origin in a rotating ring or disk. The observation of CO fundamental band absorption demands a P Cygni type geometry, i.e., an emitting area extended relative to the continuum-forming area. While emission is very dominant in the 4.6 μm HR 4049 spectrum, there is a hint of underlying and offset absorption in all the lines with the emission-line profiles having a lower peak on the blue side than on the red side. The spectrum is dominated by saturated lines 10%–20% above the continuum. However, some lines are stronger, and we assume these stronger lines result as optically thick transitions cover larger areas. At 3 μm radiation from a 550 K blackbody is about half that at 4.6 μm and, indeed, the 3 μm OH $\Delta v = 1$ lines are $\sim 5\%$ above continuum. Ultimately, saturation combined with the physical extent of the line-forming region demands a limited range of emission line strengths. The strongest lines in the 4.6 μm CO spectrum of HR 4049 are $\sim 40\%$ above the dust continuum.

The simple model of a rotating disk can be applied to the existing disk model (Fig. 1) and tested by producing model profiles of the lines. The CO first-overtone lines suggest that most of the CO occurs in a relatively thin layer. An absorption line was modeled by assuming a continuum source of 10 AU radius. The layer of absorbing gas was divided into zones of 0.1 AU along the circumference. The line rms was assumed to be 0.5 km s^{-1}, and the gas was assumed to be rotating in a Keplerian orbit. The resulting profile is a double-peaked absorption line. This profile was then convolved with a Gaussian instrumental profile with

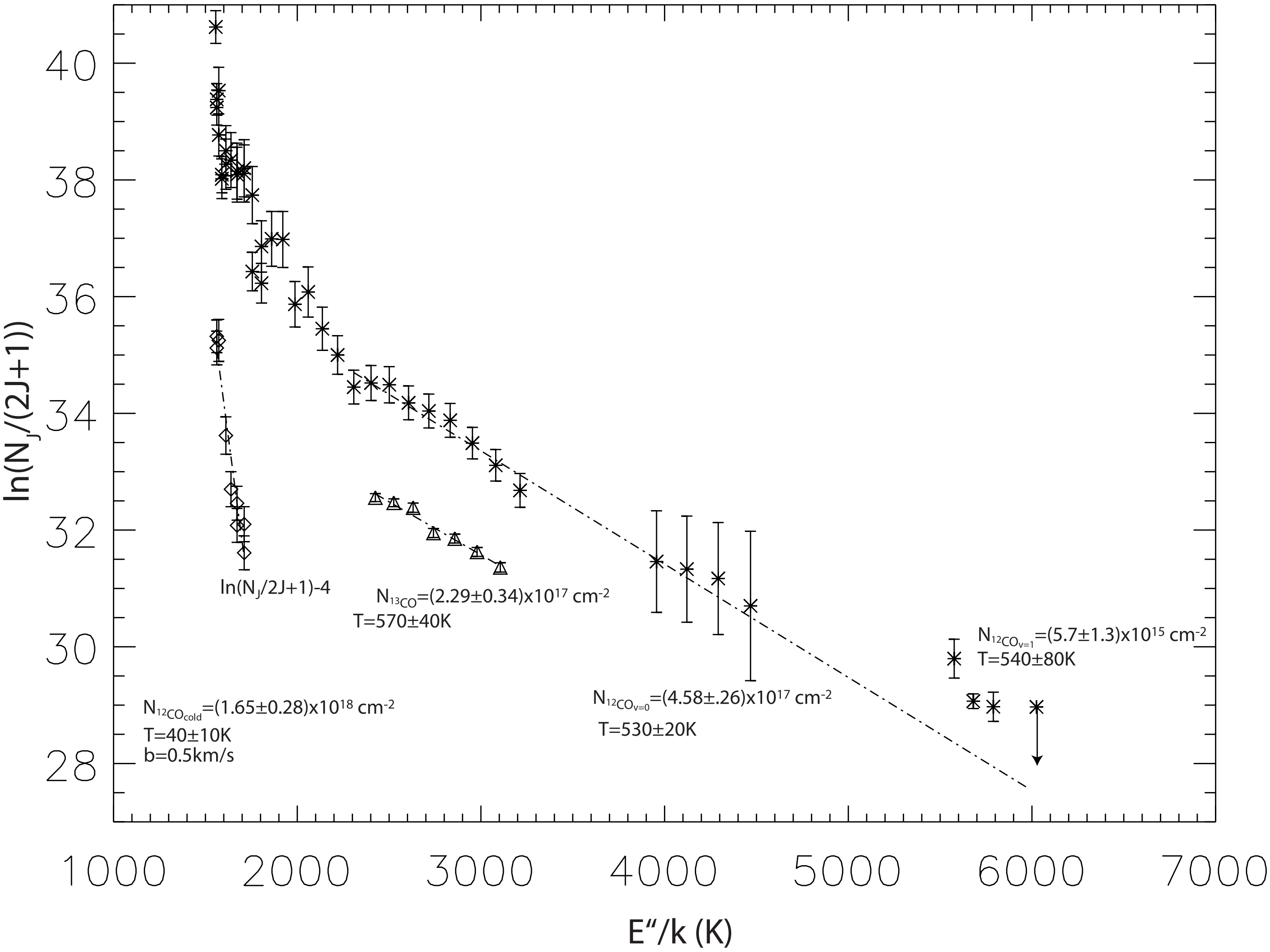

Fig. 12.—Boltzmann plot for HR 4049 first-overtone CO lines. Data are shown for the two isotopic species of CO that were detected in the first-overtone spectra, $^{12}C^{16}O$ and $^{13}C^{16}O$. The $^{12}C^{16}O$ excitation temperature is 40 ± 10 K for the low-excitation lines and 530 ± 20 K for the high-excitation 2–0 lines. The four 3–1 $^{12}C^{16}O$ lines populate the 5000–6000 K region of the abscissa with an excitation temperature of 540 ± 80 K, suggesting a slight departure from vibrational LTE. However, a fit through all higher excitation lines remains within the uncertainties and gives an excitation temperature of 620 ± 20 K. The ^{13}CO lines have an excitation temperature of 570 ± 40 K.

6 km s^{-1} FWHM. The resulting synthetic profile, which is an excellent match to observations, is shown in Figure 13.

Is this model also consistent with the 4.6 μm emission line shapes? To investigate this question five assumptions were made. (1) The emissivity of the gas is constant over the entire region modeled. (2) The gas is in Keplerian orbits. (3) Line broadening is limited to the thermal *b*-value, 0.5 km s^{-1}, discussed above and the broadening from the Keplerian motion. (4) Absorption is insignificant. (5) The gas originates at 10 AU and extends to larger radii. Since the dust disk is opaque, this extension is along the top of the disk (Fig. 1). An extension to larger radii was included, since there is no requirement for a background continuum source for the emission line spectrum. To fit the profiles with this model we found a maximum radius of 14 AU. As for the overtone model, the disk was divided into zones, the profile from each zone shifted and weighted by the viewing aspect, and then summed into velocity bins of 0.1 km s^{-1}. The resultant double-peaked profile of the emission line is seen in Figure 14. Convolution with a Gaussian instrumental profile of FWHM = 6 km s^{-1} produced a good match to a typical emission line.

While consistency between the modeled and observed profiles is satisfying, the fundamental transitions clearly require much

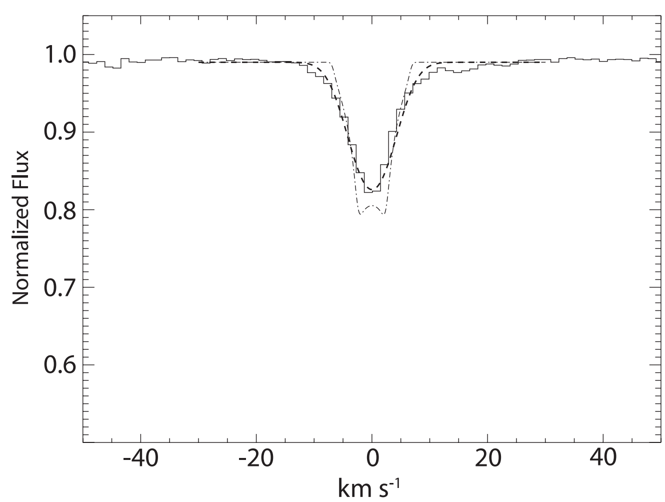

Fig. 13.—Synthetic line profiles for the CO first overtone. The dot-dashed line results from modeling a thin gas layer on the interior surface of the dust disk (see text). The dashed line is the same model spectral line convolved to the instrumental resolution. The solid line is the observed profile of the CO *R*6 line.

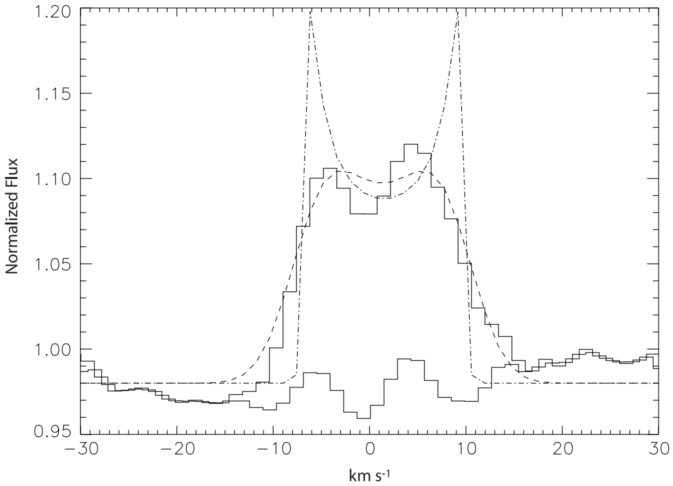

Fig. 14.—Synthetic line profile for the CO fundamental lines compared to an observed profile. The dot-dashed line is the synthetic line profile from an emitting zone near the "Cold Disk Vignetting Limit" in Fig. 1 (see text). The dashed line shows this profile convolved to the instrumental resolution. The top solid line is an observed CO line profile, and the bottom solid line is the difference between the model and observed line profile.

more refined modeling to address a number of details. For instance, there is a large difference between the 550 K CO and 1150 K dust temperatures. If, as is commonly assumed (see, e.g., Glassgold et al. 2004), the gas and dust temperatures are in equilibrium within the disk, then the 1150 K dust temperature applies only to a surface layer. Radiative cooling from CO fundamental emission (Ayres & Wiedemann 1989) is largely disabled by the large optical depth of the CO lines (Glassgold et al. 2004). It is plausible that the gas undergoes heating on exiting the disk.

In an isothermal model optically thick CO self-absorption occurs for the fundamental transitions; the opacity in the low-J 1–0 is ~400. The fundamental lines are seen in emission, because the 550 K temperature of the CO makes optically thick CO lines brighter at 4.6 μm than the 1150 K continuum. At the resolution of the observations, 6 km s^{-1}, narrow self-absorption lines of 0.5 km s^{-1} width are largely smeared out. In addition, the gas is certainly not isothermal. If, for instance, the gas is heated as it leaves the disk, the temperature profile could increase toward the observer. Depending on the details of the spatial filling, optical depth, and temperature, profile absorption is not a requirement.

Two temperatures were measured in the CO first overtone, ~40 and ~550 K, but no velocity differences were measured between the 40 and 550 K regions, suggesting that these temperature regions are physically close together. Both the 40 and 550 K CO are seen in absorption against the 1150 K continuum. H_2O, on the other hand, is seen only in emission. Emission lines are not spatially limited to the 1150 K continuum forming region. If the absence of H_2O absorption results from H_2O existing only in the disk-edge region and not in the disk midplane, the gas is differentiated vertically as well as horizontally relative to the plane of the disk.

The measured decrease in the column density in between the $v = 0$ and 1 levels implies that there is ample population to produce the observed optically thick 2–1 lines. However, the observation of optically thick 3–2 emission suggests that the $v = 3$ level is populated above that expected from LTE. Overtone transitions higher than 3–1 are outside of the region observed. It would be of interest to search for the strongest lines in the 4–2 band.

The emission profile is shifted relative to the center-of-mass velocity by ~1.5 km s^{-1}, suggesting an outflow. If the depression of the blue wing in the emission profiles is due to absorption in front of the dust disk, the absorption line profile is formed in a region with less outflow than the extended emission line forming region. Outflow was also noted for the first-overtone CO lines. The outflow increases for the very lowest excitation lines, suggesting that the gas cools in the inner-disk region and is accelerated as it flows out. For the lowest excitation CO fundamental lines the cold outflow is seen in absorption with the outflow velocity increasing (Fig. 10) as excitation energy decreases. Dominik et al. (2003) suggested that along the edges of the disk an outward flow results from radiation pressure erosion. Alternatively, a disk pressure gradient can result in an outward flow (Takeuchi & Lin 2002) without a need for small grains. Indeed, the outflow could be driven initially by either gas or dust since momentum is transferred between the gas and dust through collisions (Netzer & Elitzur 1993).

5.2. *Comparison with Optical Spectra*

A detailed analysis of time series C I, Na I D (D1 and D2), and Hα spectra of HR 4049 is presented by Bakker et al. (1998). The Na D lines contain a number of absorption components as well as weak emission. Bakker et al. (1998) identify two Na D absorption components with the circumstellar environment of the binary system. These are labeled as "A_1" and "A_2" (see Table 2 and Fig. 4 of Bakker et al. 1998). A_1 has a velocity of ~−5.0 km s^{-1} (mean of D1 and D2) relative to the systemic velocity. A_2 has a velocity of −0.8 km s^{-1} again relative to the systemic velocity. A_2 is stronger than A_1 by about 50% and has a slightly greater FWHM.

The continuum in the infrared is dominated by the dust continuum. However, in the optical the continuum is entirely from the stellar photosphere. Thus, the optical absorption is formed along a pencil beam originating near the center of the circumbinary disk. The A_1 velocity has similar velocity to the outflow seen in the lowest excitation 1–0 CO lines. This outflow is a cold wind perhaps leaving the system. The A_2 outflow is close to the outflow velocity seen in the CO first overtone as well as the slightly higher excitation 1–0 lines (Fig. 10). This flow is an outward flow of warmer gas perhaps associated with circulation in the disk.

Given that the star is the continuum source of the Na absorption and the rear inner walls of the disk are the continuum source for the CO absorption, perfect agreement is not expected in either line-of-sight velocity or in FWHM. The overtone CO has a much larger FWHM than the Na D, as expected given the larger range of velocities sampled by the CO along the lines of slight to the CO continuum–forming area (Fig. 13).

Na I also has an emission component ("A_3" in Bakker et al. 1998). This is perhaps due to fluorescent emission from the gas interior to the disk. The line profile is disrupted by the Na D absorption components, but the FWHM of the emission, ~21 km s^{-1}, is comparable to that of the CO emission.

The Hα line profile is complex. Bakker et al. (1998) identified two components, "C_{max}" and "R_{min}," which are stationary and presumably are associated with the circumbinary environment. Both are seen in absorption. The outward velocity of C_{max} is large, −21.3 km s^{-1}. The velocity of R_{min} is much less, −7.5 km s^{-1}. The energetics of the Hα line are very different from those of the cold gas lines discussed in this paper. Hα also has an absorption feature "B_{min}," which possibly varies in antiphase with the primary. Detailed understanding of the excited gas sampled by Hα requires modeling beyond the current discussion.

5.3. *Properties of the Binary Members*

The conceptual picture of a thin gas layer corotating just in front of the dust wall suggests the observed velocities result from Keplerian rotation. A FWZI of 18 km s^{-1} implies a rotational velocity of 9 km s^{-1}. Assuming Keplerian rotation and a 10 AU disk radius, the total binary mass required is 0.9 $M_{\odot}$. This is in agreement with the total binary mass suggested by Bakker et al. (1998). Bakker's mass was based on the mass function from the spectroscopic orbit and the assumption that the A supergiant had a typical white dwarf mass.

The mass function from Bakker et al. (1998), the total binary mass, and the orbital inclination allow a solution for the individual masses in the binary. We make the assumption, discussed in § 5.6, that the binary orbit is coplanar with the disk. The definition of the mass function then yields the masses for the individual stars. The A supergiant has a very low mass of 0.58 $M_{\odot}$, confirming the post-AGB state of this star. This mass, nearly equal to that of a typical white dwarf (Bergeron et al. 1992), implies that the mass-loss process for this star has terminated. The companion mass is 0.34 $M_{\odot}$. This mass does not resolve the status of the companion. While a mass of 0.34 $M_{\odot}$ is low for a white dwarf and strongly suggests an M dwarf, it is possible that the companion mass has been altered by evolution (§ 5.6).

5.4. *Winnowing*

Lambert et al. (1988) report quantitative abundances for HR 4049 revealing an extremely metal-poor star with $[Fe/H] \lesssim -3$, but near-solar C, N, and O: $[C/H] = -0.2$, $[N/H] = 0.0$, and $[O/H] = -0.5$. Lambert et al. (1988) argue that the ultralow iron abundances found in a post-AGB star cannot be primordial since there are no known progenitor AGB stars with similar abundances. Venn & Lambert (1990) and Bond (1991) find similar abundance patterns to those in HR 4049 in the young main-sequence λ Boo stars and gas in the interstellar medium (ISM). In all three cases the abundance pattern is deficient in refractory (high condensation temperature) elements but nearly solar in volatile (low condensation temperature) elements. This abundance pattern is explained in the ISM by the locking up of refractory elements in grains.

Five extremely iron-deficient post-AGB stars are known in the HR 4049 class (van Winckel et al. 1995). Lambert et al. (1988) and Mathis & Lamers (1992) have noted that all are A stars with no surface convection. A likely scenario is that the observed abundances result from peculiar abundances in little more than the observed photospheric layer. The very low refractory abundance in the HR 4049 stars results in a much lower opacity in the photospheric material than from a normal composition, making this region additionally stable against convection (Mathis & Lamers 1992). Assuming a 47 $R_{\odot}$ radius for HR 4049 (Bakker et al. 1998) and referring to a 7500 K $T_{\rm eff}$, $\log g = 1.0$ model atmosphere (Kurucz 1979), the photosphere of HR 4049 above optical depth unity contains a few percent of an Earth mass of volatile material.

Mathis & Lamers (1992) postulated that the HR 4049 abundance pattern results from the separation of mass-loss gas and dust by differential forces on the gas and dust in a circumstellar shell. Waters et al. (1992) further suggested that a circumbinary disk played a critical role. Winnowing occurs as gas is accreted to the stellar surface while dust remains in the circumstellar shell or is ejected. The λ Boo stars, which are also A stars without surface convection, have similar surface abundances due to winnowing of gas from dust in a pre–main-sequence disk (Venn & Lambert 1990). Mathis & Lamers (1992) found the removal of refractory elements from a solar abundance gas to be a very inefficient winnowing process. They suggested that an efficient winnowing process is one that creates a gas with a low refractory abundance.

Models of disks, created mainly to explore pre–main-sequence evolution, provide a rich view of the basic disk physics. While the detailed physics of the winnowing are complex, these models, combined with the current observations, reveal the basics of the winnowing process. In optically thin circumstellar regions, the radiation pressure–to–gravity ratio for A stars drags grains larger than 4 μm inward while expelling grains smaller than 4 μm (Takeuchi & Artymowicz 2001). Takeuchi & Lin (2002) extend this to disk models, showing that large particles accumulate in the inner part of the disk. These models also apply to optically thick disks where the majority of the dust in the disk is not exposed to stellar radiation (Takeuchi & Lin 2003). In this case, interaction with the stellar radiation field at the inner disk edge drives flows in the disk with the dust-to-gas ratio increasing at the inner disk edge.

Dominik et al. (2003) conclude that the grain-size distribution in the HR 4049 disk is currently indeterminate. However, they note that in the case in which the inner disk consists of small grains, these grains will be driven outward by radiation pressure, exposing a dust-free region of gas. This gas layer will be driven inward by either the gas pressure gradient or sub-Keplerian rotation. In pre–main-sequence disks it has been shown that the gas interior to the dust suffers turbulent viscosity and accretes onto the central star. The viscous timescale in pre–main-sequence circumstellar disks is typically estimated at $\sim 10^6$ yr (Takeuchi & Lin 2003; Hartmann et al. 1998).

The observations reported here of a sheet of gas at the inner disk edge support the model in which separation of volatiles from grains occurs near the inner dust disk surface. The temperature of the gas released from the grains is far too low for evaporation of refractory elements to take place. The total gas mass interior to the HR 4049 dust disk is $\sim 0.1\ M_{\oplus}$. The gas required in the stellar photosphere to alter the observed stellar abundances is one-tenth this. A naive interpretation is that the surface material required to match the observed abundances could be accreted in $\lesssim 10^5$ yr. For post-AGB evolution this may be too long. An alternative is that the winnowing process currently observed is the termination of a very rapid clearing of the inner disk region that results in sudden accretion of the gas now present in the stellar photosphere. The observed CO, H_2O, and OH is near the disk. The flow to the stellar surface is presumed much more tenuous and is not observed.

Takeuchi & Lin (2002) found that higher than a few disk scale heights from the disk midplane the gas rotates faster than the particles due to an inward pressure gradient. This drag causes particles to move outward in the radial direction. Takeuchi & Lin (2003) speculate that in an optically thick disk, particles in the irradiated surface layer move outward, while beneath the surface layer, particles move inward. The outward flow seen in CO plus the driving entrained particles could rejoin the cool outer portions of the disk. In this case, the inward interior disk flow would move this material to the inner disk surface. The winnowing process could then be a distillation process resulting in a disk with increasingly refractory grains.

5.5. *Isotopic Abundances*

The oxygen isotopic ratios reported by Cami & Yamamura (2001) set HR 4049 apart as having by a factor >10 the smallest ratios of $^{16}O/^{17}O$ and $^{16}O/^{18}O$ known at that time. Our analysis of the optically thin CO first-overtone transition does not support these results. There are no detectable $C^{17}O$ first-overtone lines giving a 3 σ limit of $^{16}O/^{17}O > 200$. On the other hand, the fundamental spectrum of CO in HR 4049 consists of optically thick emission lines. Four isotopic variants ($^{12}C^{16}O$, $^{13}C^{16}O$, $^{12}C^{17}O$, and $^{12}C^{18}O$) can be seen in the fundamental spectrum with lines of similar intensity. The CO_2 bands measured by Cami & Yamamura (2001) were observed at low resolution by *ISO* and are in the 13–17 μm region of the infrared. These bands appear in emission. We contend that the oxygen isotope ratios appear small in these CO_2 bands, because as for the CO fundamental, the emission lines are highly saturated. Cami & Yamamura (2001) warn that their isotopic ratios are in the optically thin limit.

The carbon and oxygen isotopic ratios appear typical for an AGB star (Lambert 1988). While the oxygen isotopic ratio in the circumstellar environment of HR 4049 is not abnormally low, there are stars that do have extreme oxygen isotope values. Some hydrogen-deficient carbon stars have $^{16}O/^{18}O$ considerably less than 1 (Clayton et al. 2005, 2007). Clayton et al. (2007) suggest that the extreme overabundance of ^{18}O observed in these objects is the result of He-burning in white dwarf mergers. Meteoritic samples have been found with small $^{16}O/^{18}O$ ratios. These could result from processes in the presolar nebula or pollution from a stellar source. While the rarity of stellar sources with small oxygen isotope ratios suggests a stellar source is unlikely, the origin of exotic oxygen isotopic ratios detected in early solar system samples remains uncertain (Aleon et al. 2005).

5.6. *Binary Evolution*

ISO data described by Dominik et al. (2003) contain features from oxygen-rich molecules implying that the disk is oxygen-rich. The lack of mid-infrared silicate features associated with oxygen-rich grains is attributed by Dominik et al. (2003) to high optical depth in the dust disk. Our observations reveal a 2.3–4.6 μm spectrum resulting from a mix of gas-phase molecules, CO, OH, and H_2O, typical for an oxygen-rich environment. If, as seems probable, the gas consists of volatiles evaporated from grains, then the disk environment is oxygen rich.

In contrast, as reviewed in § 1, carbon-rich circumstellar grains have been observed. An explanation is that these grains are exterior to the disk. Carbon-rich chemistry is the result of evolution in the AGB phase where CNO material processed in the stellar interior is mixed to the surface. For AGB stars of mass $\gtrsim 2$, the surface chemistry of the AGB star is converted to carbon-rich by the third dredge-up. Rapid AGB mass loss then produces a carbon-rich circumstellar shell. In the case of HR 4049 the fossil carbon-rich shell of AGB mass loss is still observable, although HR 4049 is now a post-AGB object.

Why is the disk oxygen-rich? Bakker et al. (1996) noted that the current binary separation is less than the radius required for the AGB phase of the current post-AGB star. Hence, prior to the post-AGB stage the HR 4049 system underwent common envelope evolution. Prior to the common envelope phase, the system passed through a pre-AGB contact binary phase with the more massive star transferring mass onto the less massive member. An AGB star does not contract due to mass loss, so the AGB star continued to expand, enveloping the dwarf companion. Common envelope systems rapidly eject mass from both members (Taam & Sandquist 2000). Most carbon stars have C/O near unity (Lambert et al. 1986). Mixing or mass transfer during the common-envelope stage converted the carbon-rich envelope of the AGB star back to an oxygen-rich envelope. Mass lost during the common-envelope phase formed the current circumbinary disk. In such a scenario a corotating circumbinary disk is formed surrounding the binary (Rasio & Livio 1996).

This process is apparently not unusual. De Ruyter et al. (2006) find that circumbinary disks are a common feature of post-AGB stars. The current A supergiant M dwarf HR 4049 binary is rapidly evolving to a white dwarf M dwarf binary system. White dwarf M dwarf binary systems with a cobinary disk resulting from common-envelope evolution also appear to be common (Howell et al. 2006).

6. CONCLUSIONS

The 2–5 μm spectrum of HR 4049 is formed in a circumbinary disk and wind. The optically thin 2.3 μm CO lines appear in absorption against the dust continuum, allowing the determination of the mass of gas. The gas forms a thin layer, of radial thickness $\sim 6\ R_\odot$, lining the dust disk. This gas is composed of the volatiles separated in the disk from grains. The 4.6 μm emission spectrum requires a region of line formation extended beyond the continuum-forming region. The circumbinary gas is rotating with a Keplerian velocity of ~ 9 km s^{-1}. Combined with the circumbinary disk radius and inclination derived from photometry, Keplerian rotation allows the determination of the masses of the individual binary stars. The very low mass of the A supergiant, 0.58 $M_\odot$, confirms the post-AGB nature of this object. Gas is also flowing out of the system, perhaps as a result of a disk pressure gradient, at ~ 1 km s^{-1}.

Our observations show that the HR 4049 circumbinary disk has typical AGB abundances for the carbon and oxygen isotopes; $^{12}C/^{13}C = 6^{+9}_{-4}$ and $^{16}O/^{17}O > 200$. Exotic mechanisms, as proposed, e.g., by Lugaro et al. (2005) for production of the $^{16}O/^{17}O$, are not required. The widely quoted value of $^{16}O/^{17}O \sim 8$ reported by Cami & Yamamura (2001) results from the naive interpretation that the infrared emission lines are optically thin. Cami & Yamamura (2001) warn that their values were in the optically thin limit. The extreme saturation of lines in the 4.6 μm spectrum of HR 4049 results in nearly equal apparent strengths for isotopic variants of molecular species with abundances differing by factors of 10^3.

The peculiar surface abundances of HR 4049 are likely the result of winnowing driven by the evaporation of volatiles in the disk and the viscous accretion of this gas onto the star. Detailed modeling of the process will be required to determine if there is adequate time for the current outgassing of the disk to fully explain the surfaces abundances of the A supergiant or if a sudden, post–common envelope clearing of the inner disk is required. The existence of the λ Boo stars shows that the winnowing process applies to pre–main-sequence as well as post-AGB systems. The wider significance of the winnowing process may well be in systems where the convective nature of the stellar photosphere cancels any impact on stellar abundances. However, circumstellar grains in these systems are undergoing processes separating volatile and refractory elements. This winnowing could have general application to the chemical evolution of grains in pre–main-sequence disks.

Carbon-rich circumstellar material implies that the post-AGB star was a carbon-rich star on the AGB. The current oxygen-rich circumstellar disk likely evolved from common envelope mixing. HR 4049 is one of five known post-AGB stars with similar photospheric abundances. Of the other four at least one, the red-rectangle nebula/binary HD 44179, has a similar oxygen-rich circumbinary disk in a carbon-rich circumstellar shell (Waters et al. 1998). In future papers of this series, we will explore the infrared spectra of the other members of the HR 4049 class of objects.

This paper is based in part on observations obtained at the Gemini Observatory, which is operated by the Association of Universities for Research in Astronomy, Inc., under a cooperative agreement with the NSF on behalf of the Gemini partnership: the National Science Foundation (United States), the Particle Physics and Astronomy Research Council (United Kingdom), the National Research Council (Canada), CONICYT (Chile), the Australian Research Council (Australia), CNPq (Brazil), and CONICRT (Argentina). The observations were obtained with the Phoenix infrared spectrograph, which was developed and is operated by the National Optical Astronomy Observatory. The spectra were obtained as part of programs GS-2002A-DD-1, GS-2002B-DD-1, GS-2003A-DD-1, GS-2004A-DD-1, and GS-2005B-DD-1. We thank Claudia Winge and Bernadette Rodgers and the Gemini South staff for their assistance at the telescope. We thank Richard Joyce for useful discussions. We thank the anonymous referee for a very detailed critical reading of the draft. S. D. B. acknowledges that work was performed under contract with the Jet Propulsion Laboratory (JPL) funded by NASA through the Michelson Fellowship Program. JPL is managed for NASA by the California Institute of Technology.

REFERENCES

Aleon, J., Robert, F., Duprat, J., & Derenne, S. 2005, Nature, 437, 385
Antoniucci, S., Paresce, F., & Wittkowski, M. 2005, A&A, 429, L1
Ayres, T. R., & Wiedemann, G. R. 1989, ApJ, 338, 1033
Bakker, E. J., Lambert, D. L., Van Winckel, H., McCarthy, J. K., Waelkens, C., & Gonzalez, G. 1998, A&A, 336, 263
Bakker, E. J., van der Wolf, F. L. A., Lamers, H. J. G. L. M., Gulliver, A. F., Ferlet, R., & Vidal-Madjar, A. 1996, A&A, 306, 924
Beintema, D. A., et al. 1996, A&A, 315, L369
Bergeron, P., Saffer, R. A., & Liebert, J. 1992, ApJ, 394, 228
Bond, H. E. 1991, in IAU Symp. 145, Stellar Evolution: The Photospheric Abundance Connection, ed. G. Michaud & A. Tutekov (Dordrecht: Reidel), 341
Brittain, S. D., Rettig, T. W., Simon, T., & Kulesa, C. 2005, ApJ, 626, 283
Cami, J., & Yamamura, I. 2001, A&A, 367, L1
Clayton, G. C., Geballe, T. R., Herwig, F., Fray, C., & Asplund, M. 2007, preprint (astro-ph/0703453)
Clayton, G. C., Herwig, F., Geballe, T. R., Asplund, M., Tenebaum, E. D., Engelbracht, C. W., & Gordon, K. D. 2005, ApJ, 623, L141
De Ruyter, S., Van Winckel, H., Maas, T., Lloyd Evans, T., Waters, L. B. F. M., & Dejonghe, H. 2006, A&A, 448, 641
Dominik, C., Dullemond, C. P., Cami, J., & van Winckel, H. 2003, A&A, 397, 595
Geballe, T. R., Noll, K. S., Whittet, D. C. B., & Waters, L. B. F. M. 1989, ApJ, 340, L29
Glassgold, A. E., Najita, J., & Igea, J. 2004, ApJ, 615, 972
Grevesse, N, Lambert, D. L., Sauval, A. J., van Dishoek, E. F., Farmer, C. B., & Norton, R. H. 1991, A&A, 242, 488
Guillois, O., Ledoux, G., & Reynaud, C. 1999, ApJ, 521, L133
Hartmann, L., Calvet, N., Gullbring, E., & D'Alessio, P. 1998, ApJ, 495, 385
Hinkle, K. H., & Barnes, T. 1979, ApJ, 227, 923
Hinkle, K. H., Cuberly, R., Gaughan, N., Heynssens, J., Joyce, R., Ridgway, S., Schmitt, P., & Simmons, J. E. 1998, Proc. SPIE, 3354, 810
Hinkle, K. H., Joyce, R. R., Sharp, N., & Valenti, J. A. 2000, Proc. SPIE, 4008, 720
Hinkle, K. H., et al. 2003, Proc. SPIE, 4834, 353
Howell, S. B., et al. 2006, ApJ, 646, L65
Joyce, R. R. 1992, in ASP Conf. Ser. 23, Astronomical CCD Observing and Reduction Techniques, ed. S. Howell (San Francisco: ASP), 258
Kurucz, R. L. 1979, ApJS, 40, 1
Lambert, D. L. 1988, in IAU Colloq. 106, Evolution of Peculiar Red Giant Stars, ed. H. R. Johnson & B. M. Zuckerman (Cambridge: Cambridge Univ. Press), 101
Lambert, D. L., Gustafsson, B., Eriksson, K., & Hinkle, K. H. 1986, ApJS, 62, 373
Lambert, D. L., Hinkle, K. H., & Luck, R. E. 1988, ApJ, 333, 917
Lugaro, M., Pols, O., Karakas, A. I., & Tout, C. A. 2005, Nucl. Phys. A, 758, 725
Mathis, J. S., & Lamers, H. J. G. L. M. 1992, A&A, 259, L39
McClatchey, R. A., Benedict, W. S., Clough, S. A., Burch, D. E., Calfee, R. F., Fox, K., Rothman, L. S., & Garing, J. S. 1973, AFCRL Atmospheric Absorption Line Parameters Compilation (Bedford: AFCRL)
Najita, J., Carr, J. S., Glassgold, A. E., Shu, F. H., & Tokunaga, A. T. 1996, ApJ, 462, 919
Netzer, N., & Elitzur, M. 1993, ApJ, 410, 701
Rasio, F. A., & Livio, M. 1996, ApJ, 471, 366
Smith, V. V., et al. 2002, AJ, 124, 3241
Spitzer, L. 1978, Physical Processes in the Interstellar Medium (Wiley: New York)
Taam, R. E., & Sandquist, E. L. 2000, ARA&A, 38, 113
Takada-Hidai, M. 1990, PASP, 102, 139
Takeuchi, T., & Artymowicz, P. 2001, ApJ, 557, 990
Takeuchi, T., & Lin, D. N. C. 2002, ApJ, 581, 1344
———. 2003, ApJ, 593, 524
van Winckel, H., Waelkens, C., & Waters, L. B. F. M. 1995, A&A, 293, L25
Venn, K. A., & Lambert, D. L. 1990, ApJ, 363, 234
Waelkens, C., Lamers, H. J. G. L. M., Walters, L. B. F. M., Rufener, F., Trams, N. R., LeBertre, T., Ferlet, R., & Vidal-Madjar, A. 1991a, A&A, 242, 433
Waelkens, C., Van Winckel, H., Bogaert, E., & Trams, N. R. 1991b, A&A, 251, 495
Waelkens, C., Van Winckel, H., Waters, L. B. F. M., & Bakker, E. J. 1996, A&A, 314, L17
Waters, L. B. F. M., Trams, N. R., & Waelkens, C. 1992, A&A, 262, L37
Waters, L. B. F. M., et al. 1989, A&A, 211, 208
———. 1998, Nature, 391, 868